An immersed boundary method for fluid–structure interaction with compressible multiphase flows

Author:
Wang, L; Currao, GMD; Han, F; Neely, AJ; Young, J; Tian, FB

Publication details:
Journal of Computational Physics
v. 346
pp. 131 - 151
0021-9991 (ISSN); 1090-2716 (ISSN)

Publication Date:
2017-10-01

Publisher DOI:
https://doi.org/10.1016/j.jcp.2017.06.008

An immersed boundary method for fluid–structure interaction with compressible multiphase flows

Li Wang[a,b], Gaetano M.D. Currao[b], Feng Han[a], Andrew J. Neely[b], John Young[b], Fang-Bao Tian [1b]

[a]*School of Mechatronical Engineering, Beijing Institute of Technology, Beijing 100081, China*
[b]*School of Engineering and Information Technology, University of New South Wales, Canberra ACT, 2600, Australia*

Abstract

This paper presents a two-dimensional immersed boundary method for fluid-structure interaction with compressible multiphase flows involving large structure deformations. This method involves three important parts: flow solver, structure solver and fluid–structure interaction coupling. In the flow solver, the compressible multiphase Navier–Stokes equations for ideal gases are solved by a finite difference method based on a staggered Cartesian mesh, where a fifth-order accuracy Weighted Essentially Non-Oscillation(WENO) scheme is used to handle spatial discretization of the convective term, a fourth-order central difference scheme is employed to discretize the viscous term, the third-order TVD Runge-Kutta scheme is used to discretize the temporal term, and the level-set method is adopted to capture the multi-material interface. In this work, the structure considered is a geometrically non-linear beam which is solved by using a finite element method based on the absolute nodal coordinate formulation(ANCF). The fluid dynamics and the structure motion are coupled in a partitioned iterative manner with a feedback penalty immersed boundary method where the flow dynamics is defined on an Eulerian grid and the structure dynamics is described on a global coordinate. We perform several validation cases (including fluid over a cylinder, structure dynamics, flow induced vibration of a flexible plate, deformation of a flexible panel induced by shock waves in a shock tube, an inclined flexible plate in a hypersonic flow, and shock-induced collapse of a cylindrical helium cavity in the air), and compare the results with experimental and other numerical data. The present results agree well with the published data and the current experiment. Finally, we further demonstrate the versatility of the present method by applying it to a flexible plate interacting with multiphase flows.

Key words:
Fluid–structure interaction; immersed-boundary method; viscous compressible flow; multiphase flow; large structure deformations; shock wave

1. Introduction

The fluid–structure interaction (FSI) involving compressible multiphase flow has extensive applications in industry among which examples include aeronautical engineering, coastal engineering and

[1]Correspondence author. Email addresses: f.tian@adfa.edu.au; onetfbao@gmail.com

biomedical engineering [1, 2, 3, 4]. Moreover, it is of key importance in the protection of civil engineering, such as the dynamic response of a structure under a shock load [5] and hypersonic flight [6]. Both experiment and numerical simulation have been applied to investigate such FSI problems. However, with the increase of the complexity and the spatial resolution of the engineering applications, experiments are challenging and usually too expensive. Therefore, numerical simulation has received much attention in recent decades [7]. Because of complex geometries, multi-material interface, supersonic discontinuities and large structure deformations, computational modelling of the FSI for these applications is highly challenging and thus has not been extensively explored.

There were two common ways initially designed to eliminate or reduce the oscillations near discontinuities induced in the traditional finite difference method, and based on fixed stencil interpolations [8]. One way is to add an artificial viscosity and the other is to apply limiters [9]. The essentially non-oscillatory (ENO) scheme proposed by Osher [9] chooses the appropriate stencil for the interpolation near the discontinuity to achieve a self similar, uniformly high order accurate and essential non-oscillatory interpolation. Since then, researchers have improved this methodology and expanded its applications significantly. For example, Shu and Osher [10, 11] developed ENO schemes based on points values and TVD Runge-Kutta time discretization to save computational costs; Fatemi et al. [12] and Shu [13] proposed a modified ENO method based on biased stencil to enhance the numerical stability and accuracy; Weighted ENO (WENO) schemes, developed by Jiang and Shu [14], used a convex combination of all candidate stencils instead of just one as in the original ENO. After that, WENO has been successfully applied to shock-vortex interactions [15], incompressible flows [16] and relativistic hydrodynamics [17].

When dealing with multiphase interface problems, Eulerian schemes work well for most problems and can accurately and efficiently handle large deformations characteristic of gases admitting non-physical oscillations near the multi-material interface [18]. On the other hand, purely Lagrangian methods typically result in severe mesh distortion and the consequence is ill conditioning of the element stiffness matrix leading to mesh lockup or entanglement [19]. To combine the robustness of an Eulerian scheme with a multi-material interface method characteristic of the Lagrangian scheme, Fedkiw et al. [20] proposed the ghost fluid method (GFM). In this method, the interface is traced by solving a level-set function [21, 22, 23] which gives the exact subcell interface location. By using GFM, only a band of 3 to 5 ghost cells on each side of the interface is actually needed by the computational method depending on the order of WENO method employed. However, the original ghost fluid method does not work consistently and efficiently using an isotropic fix when applied to a strong shock impacting on a multi-material interface. To overcome this difficulty, Liu et al. [24] proposed a modified ghost fluid method (MGFM) with greater robustness and consistency, where the WENO schemes were adopted in order to handle shock waves. In addition, the two-shock approximation to the Riemann problems at the multi-material interface is solved to make the MGFM less problem-related and more generally applicable.

For FSI problems involving complex geometries and large structure deformations, traditional methods based on a body conformal mesh encounter challenges in mesh generation and mesh movement [25]. The immersed boundary (IB) method developed by Peskin [26, 27] is an efficient method for this type of FSI simulations. In this method, the force acting on the fluid by the immersed boundaries is distributed onto the volumetric fluid nodes in the vicinity of the fluid–structure interface, and the force is added into the Navier–Stokes equations to achieve the boundary condition. Because of its simple boundary treatment, IB method has gained popularity for a wide range of applications [3, 4, 28, 29]. Recently, the IB method for simulating interactions between fluids and structures has received considerable attention due to its simplified grid generation requirements [4, 30]. By using the IB method, regeneration of grid is avoided, the fluid dynamics described by Eulerian variable is defined in a stationary Cartesian mesh, and the immersed boundaries are tracked in a Lagrangian system by a collection of points that move with the local fluid velocity [28]. The interaction of the fluids and structures are connected by a smoothed approximation of the Dirac delta function. The original version of the IB method was designed for natural solids (the density of the solid is the same as that of the fluid), more complications are encountered for heavy boundaries. To overcome this challenge, Zhu and Peskin [31] spread the mass of the immersed boundaries to the near Eulerian grid points in the same manner as the momentum forcing; Kim and Peskin [32] proposed a penalty IB (pIB) method, where the IB is conceptually split into two Lagrangian components: one component is massless and interacts with the fluid exactly as the traditional IB method, and the other component carrying mass is connected to the massless component by virtual stiff springs. Huang et al. [29] presented an improved version of the IB method to handle the mass of a filament. In this method, the Eulerian fluid and Lagrangian IB motion are solved independently and their interaction force is explicitly calculated using a feedback law [33]. Ghias et al. [34] and Qiu et al. [35] presented the application of the IB method to compressible flows. Marco et al. [36] studied the effects of mesh refinement in the IB method for compressible flows.

In terms of the flexible structure, both finite element method and finite difference method can be used [4, 29, 37]. In previous IB methods, the finite difference method for discretizing the 2D plate has been widely used for the FSI problem [29, 38, 39, 40]. However, the finite element method is relatively more robust and efficient for problems involving large rotation and deformation [3, 4, 37, 41]. Several finite element formulations have been proposed for the large displacement and deformation analysis of flexible multi-body systems [18, 42], including the floating frame of reference method, the incremental finite element method, the large rotation vector method and the absolute nodal coordinate formulation (ANCF). Previous studies show that the performance and efficiency of multi-body simulation codes depend largely on the coordinates selection [43, 44, 45, 46]. ANCF proposed by Shabana et al. [44, 45] which employs a set of finite element coordinates defined in the global coordinate has a superiority in handling large structure deformation and rotation. In addition, using this set of coordinates leads to a constant mass matrix which makes the procedure for implementing this formulation more efficient [47]. Therefore, ANCF has been widely used to simulate flexible multi-body system with large structure displacement and large structure deformation [48, 49].

Previous methods based on the pIB method have been designed to study flows over rigid bodies in a supersonic flow or FSI problems at low Reynolds numbers [30, 28, 29, 38, 39, 50, 40, 4, 51, 52, 35, 52, 34, 36]. Still, the existing computational simulation approaches based on the pIB method have not considered FSI problems involving shock waves, large deformations and multiphase flow. This is the motivation for this work.

In the present study, MGFM and ANCF are combined with high-order finite difference methods to simulate FSI problems involving compressible multiphase flow and large structure deformations based on the pIB method, where the fluid motion is governed by the Navier–Stokes equations and solved by MGFM, and the dynamics of the structure is governed by the dynamic equation of the geometrically nonlinear Euler-Bernoulli beam and solved by ANCF. The dynamics of the fluid and flexible structures are solved independently and the interaction force is calculated explicitly using a feedback law [33] based on the pIB method and the capture of multi-material interface in multiphase flow is achieved by using the level-set method. Such a strategy is effective in handling FSI problems involving shock waves, large structure deformations and multiphase flow as is shown in this work.

The organization of the paper is as follows. The governing equations considered are introduced in Section 2. The numerical methods are presented in Section 3 including the discrete scheme for the Navier–Stokes equations, the level-set function method used for capturing the multi-material interface, the ANCF method for the flexible structure, and the pIB method for the interaction between the fluid and structure. Validations and benchmark cases are presented in Section 4. Two applications of the present numerical method are presented in Section 5. Finally, conclusions are given in Section 6.

2. Governing equations

2.1. Navier–Stokes equations for compressible viscous flow

The flow dynamics considered here are governed by the two-dimensional compressible viscous Navier–Stokes equations

$$\frac{\partial Q}{\partial t} + \frac{\partial F}{\partial x} + \frac{\partial G}{\partial y} + \frac{1}{\mathrm{Re}}(\frac{\partial F_u}{\partial x} + \frac{\partial G_v}{\partial y}) = S, \tag{1}$$

where $Q = [\rho, \rho u, \rho v, E]^T$, $F = [\rho u, \rho u^2 + P, \rho uv, (E + P)u]^T$, $G = [\rho v, \rho uv, \rho v^2 + P, (E + P)v]^T$, $F_u = [0, \tau_{xx}, \tau_{xy}, b_x]^T$, $G_v = [0, \tau_{xy}, \tau_{yy}, b_y]^T$, $b_x = u\tau_{xx} + v\tau_{xy} - q_x$,$b_y = u\tau_{xy} + v\tau_{yy} - q_y$, S is a general source term including the external force and body force, and Re is the Reynolds number, τ_{ij} is the shear stress is defined by

$$\tau_{xx} = \frac{2}{3}\mu(2\frac{\partial u}{\partial x} - \frac{\partial v}{\partial y}), \tag{2}$$

$$\tau_{xy} = \mu(\frac{\partial u}{\partial y} + \frac{\partial v}{\partial x}), \tag{3}$$

$$\tau_{yy} = \frac{2}{3}\mu(2\frac{\partial v}{\partial y} - \frac{\partial u}{\partial x}), \tag{4}$$

and the thermal flux q_x and q_y are expressed according to Fourier's law

$$q_x = -\frac{\mu}{Pr(\gamma-1)}\frac{\partial T}{\partial x}, \quad q_y = -\frac{\mu}{Pr(\gamma-1)}\frac{\partial T}{\partial y}, \tag{5}$$

In Eq. (5), Pr is the coefficient of thermal conductivity, the temperature $T = c^2$, c is the sound speed, and γ is the adiabatic coefficient. We use $Pr = 0.72$ in the present study.

Without loss of generality, the ideal gas equation of state is used here to close the system, and thus the total energy is given by

$$E = \frac{P}{\gamma-1} + \frac{\rho(u^2+v^2)}{2}. \tag{6}$$

2.2. Structure dynamics

In present study, we consider a two-dimensional non-linear beam which is described by [29, 38]

$$\rho_s \frac{\boldsymbol{\partial X}}{\boldsymbol{\partial t}} + \frac{\partial}{\partial s}\left[(K_S|\frac{\boldsymbol{\partial X}}{\partial s}| - 1)\frac{\boldsymbol{\partial X}}{\partial s}\right] + K_B \frac{\boldsymbol{\partial X}^4}{\partial s^4} = \boldsymbol{F_f}, \tag{7}$$

where $\boldsymbol{X}$ is the Lagrangian coordinates of the flexible beam, ρ_s is linear density, K_S and K_B are respectively the tension and bending rigidity, s is the arc coordinate, and $\boldsymbol{F}_f$ is the external force acts on the beam.

3. Numerical method

3.1. Fluid solver

3.1.1. WENO for spatial dicretization of the convective term

In the fluid solver, the fifth-order accuracy WENO scheme proposed by Liu et al. [53] is used for the spatial discretization of the convective term. The procedure of descretizing the convective term $\partial F \partial x$ in Navier-Stokes equations ($\partial G/\partial y$ can be treated by the same method) is briefly introduced as follows:

(1) The mean numerical flux $\tilde{Q}$ and $\tilde{F}$ at grid $j+1/2$ is evaluated by Roe average [20].

(2) Let $A = \partial\tilde{F}/\partial\tilde{U} = R\Lambda L$, $\Lambda = diag(u-c, u, u, u+c)$, then project the flux Q and F on local characteristic space: $q = L_{j+1/2}Q$, and $f = L_{j+1/2}F$.

(3) The characteristic flux f is split into both positive and negative parts by Lax-Friedrich's splitting, $f^{\pm} = \frac{1}{2}(f \pm \lambda_{max} q)$, where $\lambda_{max} = max(\Lambda)$.

(4) The fifth-order WENO scheme is used to construct the flux $f^{\pm}$: $\hat{f}_{j+1/2} = \hat{f}^{+}_{j+1/2} + \hat{f}^{-}_{j+1/2}$, where $\hat{f}^{+}_{j+1/2}$ is constructed by

$$\hat{f}^{+}_{j+1/2} = \omega_1 f^{(1)}_{j+1/2} + \omega_2 f^{(2)}_{j+1/2} + \omega_3 f^{(3)}_{j+1/2}, \tag{8}$$

$$f^{(1)}_{j+1/2} = 1/3 f_{j-2} - 7/6 f_{j-1} + 11/6 f_j, \tag{9}$$

$$f^{(2)}_{j+1/2} = -1/6 f_{j-1} + 5/6 f_{j-1} + 1/3 f_{j+1}, \tag{10}$$

$$f^{(3)}_{j+1/2} = 1/3 f_j + 5/6 f_{j+1} - 1/6 f_{j+2}, \tag{11}$$

with the weight factors being

$$\omega_k = \frac{\alpha_k}{\alpha_1 + \alpha_2 + \alpha_3}, \quad \alpha_k = \frac{C_k}{(\varepsilon + IS_k)^2}, \quad k = 1, 2 \text{ and } 3, \quad \varepsilon = 10^{-6}, \tag{12}$$

$$IS_1 = \frac{1}{4}(f_{j-2} - 4f_{j-1} + 3f_j)^2 + \frac{13}{12}(f_{j-2} - 2f_{j-1} + f_j)^2, \tag{13}$$

$$IS_2 = \frac{1}{4}(f_{j-1} - f_{j+1})^2 + \frac{13}{12}(f_{j-1} - 2f_j + f_{j+1})^2, \tag{14}$$

$$IS_3 = \frac{1}{4}(3f_j - 4f_{j+1} + f_{j+2})^2 + \frac{13}{12}(f_j - 2f_{j+1} + f_{j+2})^2. \tag{15}$$

The construction for $\hat{f}^{-}_{j+1/2}$ is similar.

(5) Through a reverse transformation, i.e. $\hat{F}_{j+1/2} = R_{j+1/2}\hat{f}_{j+1/2}$, the discretization of the flux F can be written as

$$\left(\frac{\partial F}{\partial x}\right)_j = \frac{\hat{F}_{j+1/2} - \hat{F}_{j-1/2}}{\Delta x}. \tag{16}$$

3.1.2. Spatial discretization of the viscous term

For the viscous term, a fourth-order central difference scheme is used to discretize the spatial derivatives

$$\left(\frac{\partial F_u}{\partial x}\right)_i = \frac{1}{12}[-(F_u)_{i+2} + 8(F_u)_{i+1} - 8(F_u)_{i-1} + (F_u)_{i+2}]. \tag{17}$$

A fourth-order inward difference scheme is used for the discretization of viscous term on the out boundary, i.e. for left and bottom boundary

$$\left(\frac{\partial F_u}{\partial x}\right)_i = \frac{1}{6}[-11(F_u)_i + 18(F_u)_{i+1} - 9(F_u)_{i+2} + 2(F_u)_{i+3}], \tag{18}$$

and for right and top boundary

$$\left(\frac{\partial F_u}{\partial x}\right)_i = \frac{1}{6}[11(F_u)_i - 18(F_u)_{i-1} + 9(F_u)_{i-2} - 2(F_u)_{i-3}]. \tag{19}$$

3.1.3. Modified ghost fluid method

The ghost fluid method(GFM) presented a fairly simple way for the extension to multi-dimensions. The propagation of a shock wave in two-phase fluid is related to the strong shock on the multi-material interface, which causes inapplicability of original GFM. In order to handle the strong shock impacting on the multi-material interface, a MGFM is established by Liu [24]. This method solves a two-shock approximation to the *Riemann* problem at the interface. The details of MGFM can be found in Ref. [24].

In the MGFM, the level set technique is employed to capture the moving interface,

$$\phi_t + u\phi_x + v\phi_y = 0. \tag{20}$$

Similar to the Navier–Stokes equations, the fifth-order WENO scheme is employed to discretize the convective term of the level-set equation spatially. Specifically, for grid point i, the constructions of ϕ_x^- and ϕ_x^+ can be achieved by

$$(\phi_x^{\pm})_i = \omega_1\left(\frac{\nu_1}{3} - \frac{7\nu_2}{6} + \frac{11\nu_3}{6}\right) + \omega_2\left(-\frac{\nu_2}{6} + \frac{5\nu_3}{6} + \frac{\nu_4}{3}\right) + \omega_1\left(\frac{\nu_3}{3} + \frac{5\nu_4}{6} - \frac{\nu_5}{6}\right), \tag{21}$$

$$a_j = \frac{C_j}{(\varepsilon + IS_j)^2}, \quad \omega_j = \frac{a_j}{a_1 + a_2 + a_3}, \quad j = 1, 2 \text{ and } 3, \quad \varepsilon = 10^{-6}, \tag{22}$$

where

$$\nu_j = \frac{\phi_{i-3-j} - \phi_{i-4-j}}{\Delta x}, \quad j = 1, 2, .., 5, \text{ for } \phi_x^-, \tag{23}$$

$$\nu_j = \frac{\phi_{i+4-j} - \phi_{i+3-j}}{\Delta x}, \quad j = 1, 2, .., 5, \text{ for } \phi_x^+, \tag{24}$$

$$IS_1 = \frac{13}{12}(\nu_1 - 2\nu_2 + \nu_3)^2 + \frac{1}{4}(\nu_1 - 4\nu_2 + 3\nu_3)^2, \tag{25}$$

$$IS_2 = \frac{13}{12}(\nu_2 - 2\nu_3 + \nu_4)^2 + \frac{1}{4}(\nu_2 - \nu_4)^2, \tag{26}$$

$$IS_3 = \frac{13}{12}(\nu_3 - 2\nu_4 + \nu_5)^2 + \frac{1}{4}(3\nu_3 - 4\nu_4 + \nu_5)^2. \tag{27}$$

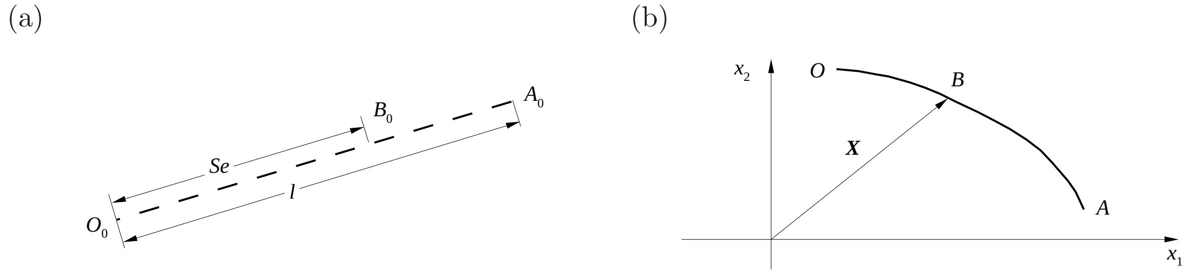

Figure 1: A schematic illustration: (a) an element and (b) deformed beam.

When the velocity in Eq. (20) $u > 0$, ϕ_x^+ is used as ϕ_x, otherwise ϕ_x^- is used. The discretization of ϕ_y is as for ϕ_x.

As Eq. (20) moves the level set $\phi = 0$ at the correct velocity, ϕ is not a distance function(i.e. $|\nabla\phi| \neq 1$). In this case, an iteration method introduced by Sussman [22] is used to reinitialize ϕ, which is achieved by solving the following equations until the steady state is obtained

$$\phi_t = \eta(\phi_0)(1 - \sqrt{\phi_x^2 + \phi_y^2}), \quad \phi(\boldsymbol{x}, 0) = \phi_0(\boldsymbol{x}), \tag{28}$$

where η is the sign function defined as

$$\eta(\phi_0) = \frac{\phi_0}{\sqrt{\phi_0^2 + \varepsilon_x^2}}. \tag{29}$$

Here ε_x equals the minimum grid length to avoid the division by zero error. The fifth-order WENO scheme described above is used to discretize Eq. (28).

3.1.4. Temporal discretization method

For all unsteady equations involved in flow solver, the third-order TVD Runge-Kutta method is used for time discretization [10]

$$Q^{(1)} = Q^{(n)} + \Delta t RHS(Q^{(n)}), \tag{30}$$

$$Q^{(2)} = \frac{3}{4}Q^{(n)} + \frac{1}{4}(Q^{(1)} + \Delta t RHS(Q^{(1)})), \tag{31}$$

$$Q^{(n+1)} = \frac{1}{3}Q^{(n)} + \frac{2}{3}(Q^{(2)} + \Delta t RHS(Q^{(2)})). \tag{32}$$

3.2. Structure solver

According to the virtual work principle, the dynamic equation of the flexible beam can be rewritten as

$$\boldsymbol{\delta W_i} + \boldsymbol{\delta W_f} + \boldsymbol{\delta W_e} + \boldsymbol{\delta W_b} = \boldsymbol{0}, \tag{33}$$

where $\boldsymbol{\delta W_i}$ is the virtual work of inertial force, $\boldsymbol{\delta W_f}$ is the virtual work of external force, $\boldsymbol{\delta W_e}$ is the virtual work of elastic force, and $\boldsymbol{\delta W_b}$ is the virtual work of bending moment.

In an inertial coordinate system as shown in Fig 1, the global position vector $\boldsymbol{X}$ of an arbitrary point on a beam element of length l is defined in terms of the nodal coordinates and the element shape function [54]

$$\boldsymbol{X} = [X_1, X_2]^T = \boldsymbol{N}\boldsymbol{e}, \tag{34}$$

where $\boldsymbol{N}$ is the shape function and $\boldsymbol{e}$ is the vector of element nodal coordinates is expressed as

$$\boldsymbol{e} = [e_1, e_2, e_3, e_4, e_5, e_6, e_7, e_8]^T. \tag{35}$$

This vector of absolute nodal coordinates includes the global displacements

$$e_1 = X_1|_{s_e=0}, \quad e_2 = X_2|_{s_e=0}, \quad e_5 = X_1|_{s_e=l}, \quad e_6 = X_2|_{s_e=l}, \tag{36}$$

and the global slopes of the element nodes that are defined as

$$e_3 = \frac{\partial X_1}{\partial s_e}|_{s_e=0}, \quad e_4 = \frac{\partial X_2}{\partial s_e}|_{s_e=0}, \quad e_7 = \frac{\partial X_1}{\partial s_e}|_{s_e=l}, \quad e_8 = \frac{\partial X_2}{\partial s_e}|_{s_e=l}, \tag{37}$$

where s_e is the arc length coordinate of an arbitrary point on the element in the undeformed configuration.

The shape function in Eq. (34) is defined by [45]

$$\boldsymbol{N} = [\boldsymbol{N_1}, \boldsymbol{N_2}], \tag{38}$$

where

$$\boldsymbol{N_1} = \begin{bmatrix} [1 - 3\xi^2 + 2\xi^3 & 0 & l(\xi - 2\xi^2 + \xi^3) & 0 \\ 0 & 1 - 3\xi^2 + 2\xi^3 & 0 & l(\xi - 2\xi^2 + \xi^3) \end{bmatrix}, \tag{39}$$

$$\boldsymbol{N_2} = \begin{bmatrix} [3\xi^2 - 2\xi^3 & 0 & l(\xi^3 - \xi^2) & 0 \\ 0 & 3\xi^2 - 2\xi^3 & 0 & l(\xi^3 - \xi^2) \end{bmatrix}, \quad \xi = s_e/l. \tag{40}$$

According to the generalized virtual work principle and the Euler-Bernoulli equation of the beam, the generalized mass matrix, stiffness matrix and body force of an element can be respectively written as

$$\boldsymbol{M_{ff}} = \rho_s \int_0^l \boldsymbol{N^T N} ds, \tag{41}$$

$$\boldsymbol{K_{ff}} = K_B \int_0^l \boldsymbol{N_{ss}^T N_{ss}} ds - \frac{K_S}{2} \int_0^l \boldsymbol{N_s^T N_s} ds + \frac{K_S}{2} \int_0^l \boldsymbol{e^T N_s^T N_s e N_s^T N_s} ds, \tag{42}$$

$$\boldsymbol{F_d} = \rho_s \int_0^l \boldsymbol{N^T} [0, g]^T ds, \tag{43}$$

where g is the acceleration of gravity, and $\boldsymbol{F_d}$ is the body force.

The structure global generalized mass matrix $\boldsymbol{M_f}$, stiffness matrix $\boldsymbol{K_f}$, external force vector $\boldsymbol{Q_f}$ and nodal coordinates vector $\boldsymbol{Q_e}$ can be obtained by assembling the corresponding element matrices using a standard finite element procedure. Consequently, the virtual work of generalized inertial force, internal force (including tension force and bending moment) and external force can be written as

$$\boldsymbol{\delta W_i} = -\boldsymbol{M_f \ddot{Q}_e \delta Q_e}, \quad \boldsymbol{\delta W_e} + \boldsymbol{\delta W_b} = -\boldsymbol{K_f Q_e \delta Q_e}, \quad \boldsymbol{\delta W_f} = \boldsymbol{Q_f Q_e \delta Q_e}. \tag{44}$$

By applying Eq. (44) in Eq. (33), then the dynamic equation can be written as

$$\boldsymbol{M_f}\ddot{\boldsymbol{Q}}_{\boldsymbol{e}} + \boldsymbol{K_f}\boldsymbol{Q_e} = \boldsymbol{Q_f}, \tag{45}$$

where $\ddot{\boldsymbol{Q}}_{\boldsymbol{e}}$ is the generalized acceleration vector (second order time derivatives of the nodal coordinates). Eq. (45) is solved by the Gauss-Seidel iteration method [54], and central difference method is used for the temporal discretization.

3.3. IB method for the fluid-structure interaction

The interaction force between the fluid and the structure can be determined by the feedback law [32]

$$\boldsymbol{F}_f = \alpha \int_0^t (\boldsymbol{U}_{ib} - \boldsymbol{U})dt + \beta(\boldsymbol{U_{ib}} - \boldsymbol{U}), \tag{46}$$

where $\boldsymbol{U}_{ib}$ is the boundary velocity obtained by interpolation at the IB, $\boldsymbol{U}$ is the structure velocity calculated from FEM, and α and β are large positive free constants. Details of choosing α and β can be found in Ref. [29]. The force acting on the Lagrange structure from the ambient fluid can be taken as a concentrated force acting on the corresponding nodes, and thus it can be added to the general force $\boldsymbol{Q_f}$ in Eq. (45).

The transformation between the Euler and Lagrange variables can be realized by the Dirac delta function. The interpolation of velocity and the spreading of the Lagrange force to the adjacent grid points are expressed as

$$\boldsymbol{U}_{ib}(s,t) = \int_\Omega \boldsymbol{u}(x,t)\delta_h(\boldsymbol{X}(s,t) - \boldsymbol{x})d\boldsymbol{x}, \tag{47}$$

$$\boldsymbol{f}(\boldsymbol{x},t) = -\int_\Gamma \boldsymbol{F}_f(s,t)\delta_h(\boldsymbol{X}(s,t) - \boldsymbol{x})ds, \tag{48}$$

where $\boldsymbol{u}$ is the fluid velocity, $\boldsymbol{x}$ is the coordinates of fluid, and Ω is the fluid domain and Γ is the structure domain.

The smooth function δ_h is used to approximate the Dirac delta function

$$\delta_h(x,y) = \frac{1}{h^2}\lambda(\frac{x}{h})\lambda(\frac{y}{h}). \tag{49}$$

In this paper, the four-point delta function introduced by Peskin[8] is used

$$\lambda(r) = \begin{cases} \frac{1}{8}(3 - 2|r| + \sqrt{1 + 4|r| - 4|r|^2}), & 0 \le |r| < 1, \\ \frac{1}{8}(5 - 2|r| - \sqrt{-7 + 12|r| - 4|r|^2}), & 1 \le |r| < 2, \\ 0, & 2 \le |r|. \end{cases} \tag{50}$$

The force $\boldsymbol{f}$ in Eq. (48) acts on the fluid by the Lagrange structure can be decomposed in x and y direction, i.e. f_x and f_y. Consequently, $\boldsymbol{S}$ on the right-hand side of the Navier–Stokes equations can be rewritten as

$$\boldsymbol{S} = [0, f_x, f_y, uf_x + vf_y]^T. \tag{51}$$

3.4. *Summary of the numerical method*

The integrated algorithm can be summarized as follows. Given all values at time step n, the values at time step $n+1$ can be updated by

(1) Calculate $\boldsymbol{U}_{ib}$ by using Eq. (47), and then update the Lagrangian force $\boldsymbol{F}_f$ by using Eq. (46);

(2) Spread the Lagrangian force $\boldsymbol{F}_f$ onto the ambient fluid nodes by using Eq. (48);

(3) Solve level-set function Eq. (20) and *Riemann* problem at the interface if multiphase flow with shock wave is considered, otherwise skip the step;

(4) Solve Eq. (1) to update flow field;

(5) Update $\boldsymbol{Q_e}$ and $\dot{\boldsymbol{Q}}_{\boldsymbol{e}}$ by solving Eq. (45).

4. Validation of the numerical method

4.1. *A uniform flow over a stationary cylinder*

In order to validate the present fluid solver in combination with the feedback force law, the uniform flow over a stationary cylinder is simulated. The computational domain for the flow is a rectangular box extending from $(-10D, -15D)$ to $(35D, 15D)$, where D is the diameter of the cylinder. The grid size of the fluid and the cylinder are set as $0.04D$ and $0.02D$, respectively. The initial velocity is set as the far field velocity u_∞ everywhere in the fluid domain. To maintain the far field boundary condition, the velocity in a thin vertical strip running along the left-hand (inflow) side of the computational domain is modified at each time step to be u_∞ [55]. Additionally, we set a large initial pressure of the fluid to make a low Mach number (< 0.1), so that the compressibility of the fluid is ignorable, and the flow can be taken as incompressible. Consequently, there is only one non-dimensional parameter, the Reynolds number, which is defined as

$$\mathrm{Re} = \frac{\rho u_\infty L}{\mu}. \tag{52}$$

In order to discuss the hydrodynamic force characteristics of the cylinder, the non-dimensional drag and lift coefficients are defined as

$$C_D = \frac{F_D}{0.5\rho u_\infty^2 L}, \quad C_L = \frac{F_L}{0.5\rho u_\infty^2 L}, \tag{53}$$

where F_D and F_L are respectively the drag and lift forces. In the present computation, F_D and F_L are integrated from the force acts on the IB by the ambient fluid

$$F_D = \int F_x ds = \sum_{i=1}^{n} F_x^i \Delta s, \quad F_L = \int F_y ds = \sum_{i=1}^{n} F_y^i \Delta s, \tag{54}$$

where F_x^i and F_y^i are respectively the force acting on the *i-th* IB point in x and y direction, and Δs is the mesh length of the rigid cylinder. Two different Reynolds numbers, 40 and 100, are considered. The first case corresponds to a steady flow regime and the second one to unsteady flow. For Re=40, the geometrical properties of the symmetrical vortices (as defined in Fig. 2) and C_D are computed and shown in Table 1. For comparison, the data from literature are shown in Table. 1. It shows good agreement between the present simulation and previous results.

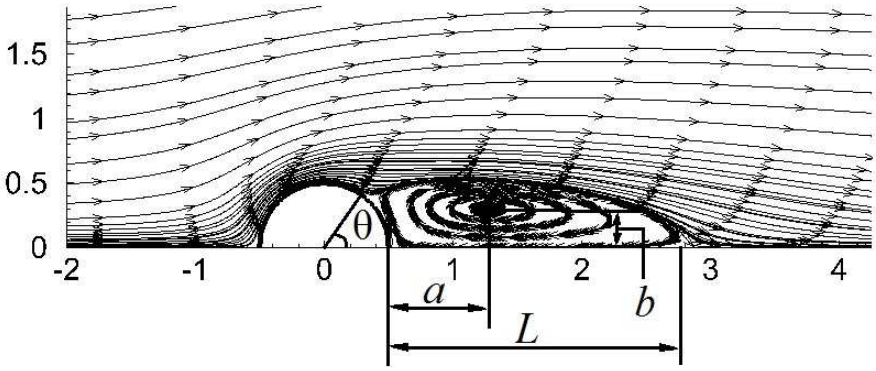

Figure 2: The stream lines for Re = 40 and definitions of quantities used in Table 1.

Table 1: A uniform flow over a stationary cylinder for Re=40: length L of recirculation zone, location (a, b) of vortex center, separation angle and drag coefficient C_D.

Sources	L/D	a/D	$2b/D$	θ	C_D
Present result	2.29	0.75	0.60	52.1^o	1.65
Linnick and Fasel [56]	2.28	0.72	0.60	53.6^o	1.54
Russell and Wang [57]	2.29	–	–	53.1^o	1.60
Herfjord [58]	2.25	0.71	0.60	51.2^o	1.60
Berthelsen and Faltinsen [59]	2.29	0.72	0.60	53.9^o	1.59
Xu and Wang [60]	2.21	–	–	53.5^o	1.66

For Re=100, the Strouhal number is introduced to characterize the vortex shedding frequency, St=$D/(u_\infty T)$. St, the average drag coefficient $C_{D,m}$ and lift coefficient C_L are presented in Table 2 with numerical and experimental results available in literature. The drag and lift coefficients history with non-dimensional time are plotted in Fig. 3. Fig. 4 presents the snapshot of the vorticity contours for Re=100 at a non-dimensional time of 250. It is found that the present predictions are in a good agreement with previous data, showing the reliability of the fluid solver and the pIB method used in this paper for viscous flow.

It should be noted that, for such a low Mach number ($M_a < 0.1$), it is not necessary to use the WENO scheme, and numerical experiments show that the difference between results using WENO and other finite difference methods is ignorable.

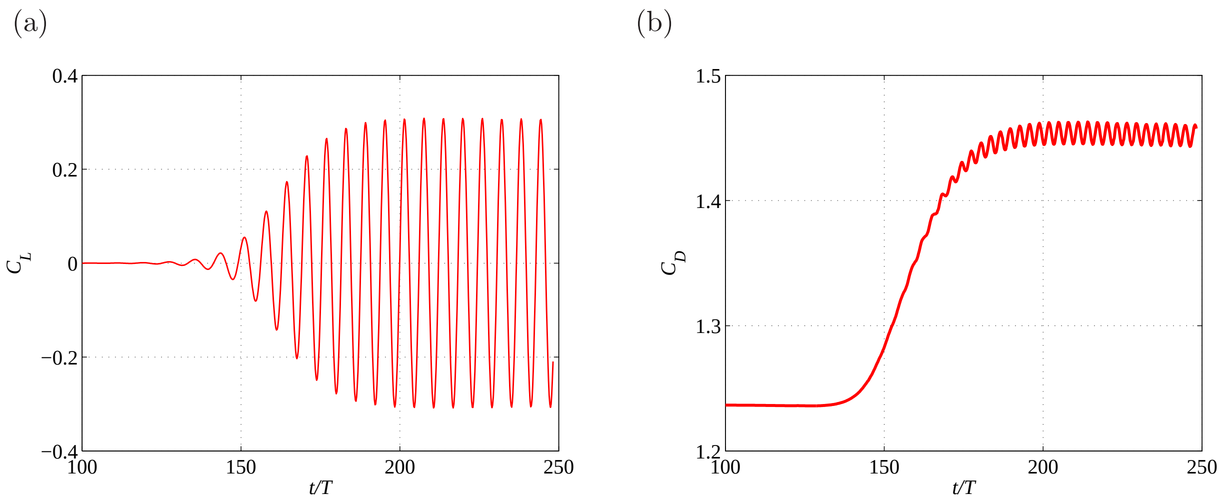

Figure 3: Lift (a) and drag (b) coefficient histories for Re=100.

Table 2: A uniform flow over a stationary cylinder for Re=100: Strouhal number St, drag coefficient $C_{D,m}$ and lift coefficient C_L.

Sources	St	$C_{D,m}$	C_L
Present result	0.161	1.44	0.31
Williamson [61]	0.164	–	–
Le et al. [62]	0.160	1.37	0.32
Herfjord [58]	0.168	1.36	0.34
Xu and Wang [60]	0.171	1.42	0.34
Berthelsen and Faltinsen [59]	0.169	1.38	0.34
Calhoun [63]	0.175	1.33	0.30
Tian et al. [50]	0.166	1.43	–

4.2. A hanging filament in vacuum

In this section, the motion of a hanging filament in vacuum under a gravitational force is conducted to validate the ANCF structure solver. The filament is initially held stationary at an angle from the horizontal, as a result, the initial generalized coordination of element i of the plate can be written as

$$e|_i = [(i-1)l, 0, cos\alpha_0, sin\alpha_0, il, 0, cos\alpha_0, sin\alpha_0]^T. \tag{55}$$

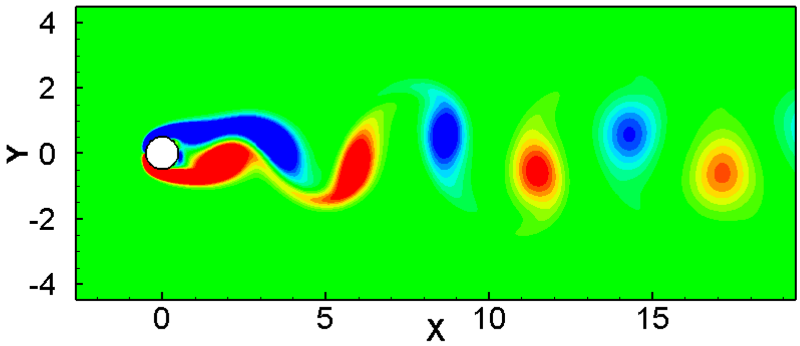

Figure 4: Snapshot of the vorticity contours for Re=100. The vorticity ranges from $-u_\infty/D$ to u_∞/D.

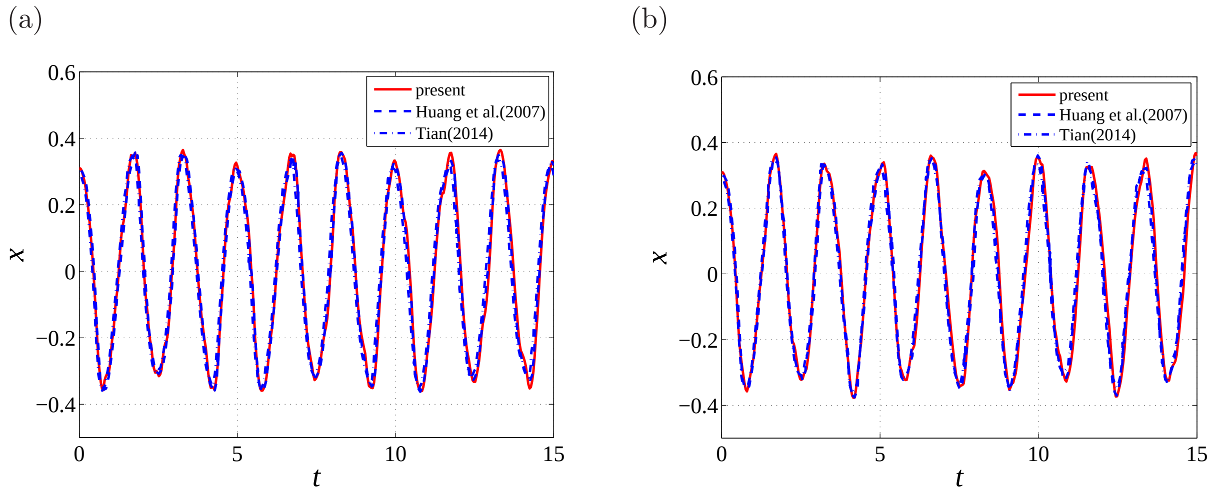

Figure 5: Horizontal coordinate histories of the free end of the filament: (a) K_B^*=0, and (b) K_B^*=0.01.

In this simulation, we use the length of the filament $L = 1.0$, $\alpha_0 = -0.4\pi$, the element length $l = 0.01L$, the reference density $\rho = 1.0kg/m^2$ and velocity $u_\infty = 1.0m/s$. Please note that ρ and u_∞ are arbitrary for scaling purposes. The non-dimensional parameters controlling this problem are defined as follows

$$\mathrm{Fr} = \frac{g}{u_\infty^2 L}, \quad K_S^* = \frac{K_S}{\rho u_\infty^2 L^2}, \quad K_B^* = \frac{K_B}{\rho u_\infty^2 L^3}, \quad m^* = \frac{\rho_s}{\rho L}. \tag{56}$$

Two different bending rigidities are simulated for $m^* = 1.0$, $\mathrm{Fr} = 10$, $K_S^* = 1000$: $K_B^* = 0.00$ and 0.01. The free end position of the filament in the horizontal direction is presented in Fig. 5 with the available data from Refs. [29, 64]. The behaviours of the filament with these two different bending rigidities have been discussed by Huang et al. [29] and Tian [64], showing that the time histories of the free end position exhibit little difference for the two cases as shown in Fig. 5. The quantitative comparison in Fig. 5 shows that the present results are in good agreement with the published data.

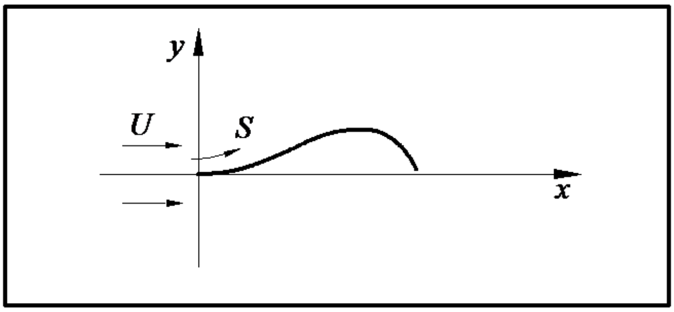

Figure 6: Schematic of a highly flexible plate in a uniform flow.

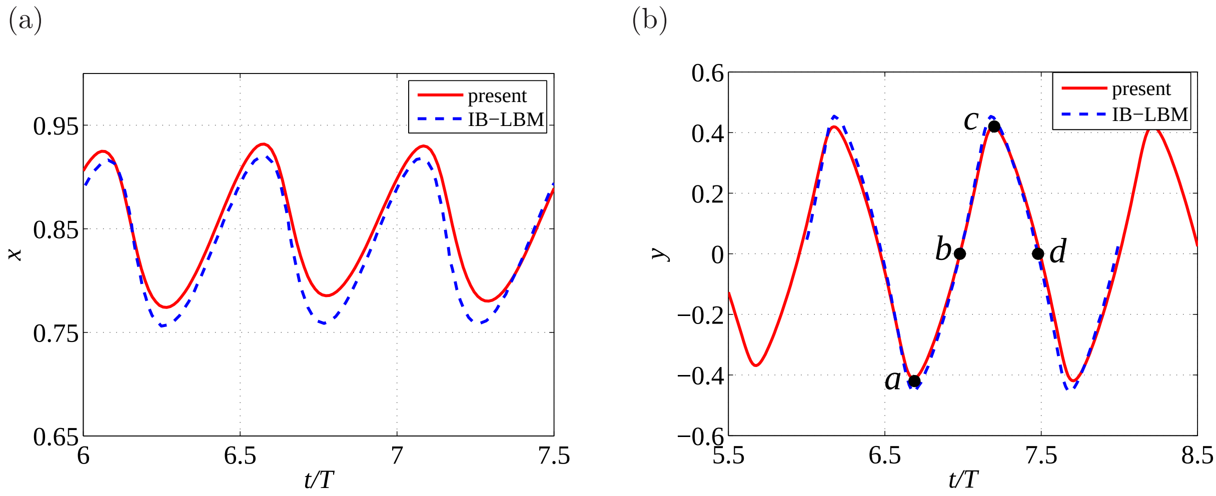

Figure 7: x-coordinate (a) and y-coordinate (b) of the trailing end of a plate flapping in a uniform flow.

4.3. Flow induced vibration of a highly flexible plate in a uniform flow

In this section, we consider a highly flexible plate of length $L = 1.0$ with one end fixed in a uniform flow, as shown in Fig. 6, to validate the present FSI solver. The computational domain for the flow is a rectangular box extending from $(-5L, -3L)$ to $(10L, 3L)$, and the mesh size for the fluid and the flexible plate are $0.02L$ and $0.01L$, respectively. The non-dimensional parameters governing the motion of the plate are

$$\mathrm{Re} = \frac{\rho u_\infty L}{\mu}, \quad m^* = \frac{\rho_s}{\rho L}, \quad K_S^* = \frac{K_S}{\rho u_\infty^2 L^2}, \quad K_B^* = \frac{K_B}{\rho u_\infty^2 L^3}, \tag{57}$$

The computational parameters are set as Re=100, $m^* = 1, K_S^* = 500$ and $K_B^* = 0.0001$.

Simulations are conducted until the vibration of the plate is periodic. For the purpose of comparison, we present the $x-$coordinate and $y-$coordinate of trailing end calculated by the penalty IB–lattice Boltzmann method (IB–LBM) [38, 39, 40, 50, 65] in Fig. 7. This shows that the coordinates of the trailing end agree well with those predicted by the IB-LBM. We also note discrepancies during fast transient periods. Specifically, the error of $y-$coordinate between present method and the IB-LBM is about 5%. The asymmetric behavior when the amplitude of the plate moves from the minimum to

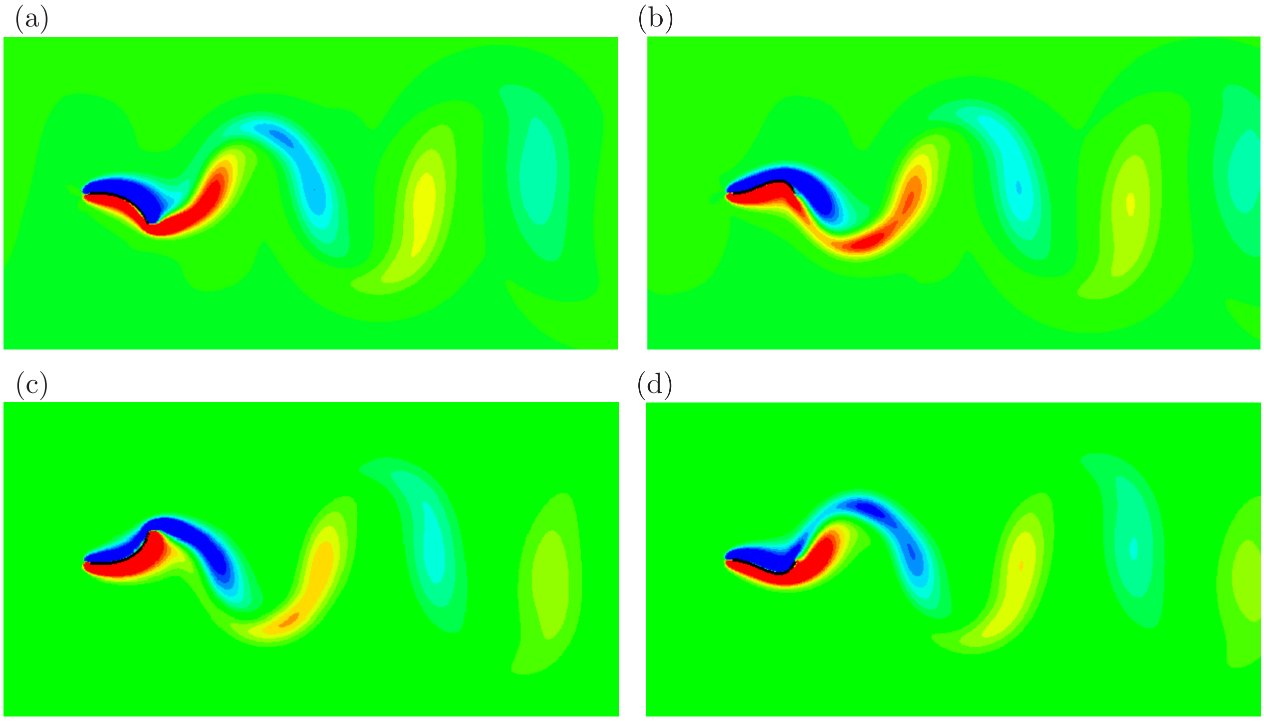

Figure 8: Vorticity contours of a plate flapping in a uniform flow at four typical instants as indicated in Fig. 7(a). The vorticity ranges from $-3u_{\infty}/L$ to $3u_{\infty}/L$.

the maximum is captured by both methods, which was discussed for flags by Connell et al. [66]. The Strouhal number which characterizes the flapping shedding frequency defined as $\mathrm{St}=L/(u_{\infty}T)$ is 0.288 in the present simulation, while that predicted by IB–LBM is 0.299 (a difference is about 3%). Finally, the vorticity contours at four instants as indicated in Fig. 7(a) are presented in Fig. 8. Such flow characteristics are consistent with those in Ref. [66].

4.4. Deformation of a flexible panel induced by a shock wave

In this section, we calculate the deformation of a panel induced by a shock wave in a shock tube as shown in Fig. 9. This problem was firstly proposed by Giordano et al. [67] in an experiment, and then numerically studied by Deiterding and Cirak et al. [68, 69]. The thickness h and the length L of the panel are respectively $1mm$ and $50mm$. The panel is clamped into a forward-facing step mounting. The geometrical parameters are $l_1 = 400mm$, $l_2 = 130mm$, $l_3 = 265mm$, $l_4 = 250mm$, $H = 80mm$ and $h_1 = 15mm$. The inflow boundary conditions are applied on the left-hand side and rigid wall boundary conditions anywhere else. The forward-facing step geometry is also represented by a fixed (rigid) boundary in the simulation. Please note that the turbulence does not play a dominating role because the initial flow around the panel is quiescent and exploration time is relatively short [67]. Therefore, we do not use a turbulence model.

The initial parameters are set as follows: $\rho_1 = 1.6548kg/m^3$, $u_1 = 112.61m/s$, $v_1 = 0$, $P_1 = 156.18KPa$, $\rho_2 = 1.2kg/m^3$, $u_2 = 0$, $v_2 = 0$, $P_2 = 100KPa$ and $\gamma = 1.4$. The material parameters for

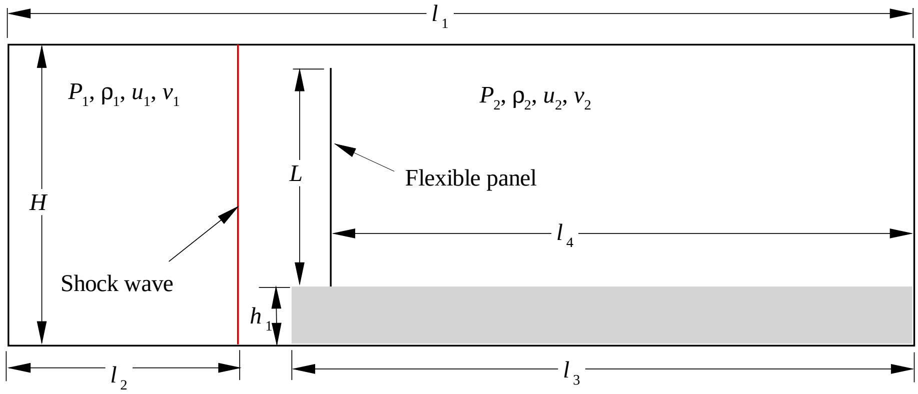

Figure 9: Geometry of the computational set-up for the shock-panel interaction in a shock tube.

the panel are density $\rho_p = 7600kg/m^3$ and elastic modulus $E_s = 220GPa$. The density ρ_2, initial sound speed $c_2 = \sqrt{\gamma P_2/\rho_2} = 341.56m/s$ and the initial length of the panel $L = 50mm$ are used for the scaling treatment. The non-dimensional computational domain expands from $(-2.4L, 0)$ to $(5.6L, 1.6L)$, the mesh size for the fluid and panel are respectively $0.01L$ and $0.005L$. Other non-dimensional parameters are $\rho_1^* = 1.3715$, $u_1^* = 0.3297$, $P_1^* = 1.1156$, $\rho_2^* = 1.0, P_2^* = 0.7143$, $K_S^* = 3.14 \times 10^4$, $\nu = 0.33$ and $K_B^* = 1.1734$.

In Fig. 10, the Schliren pictures (contours of amplitude of density gradient) from the present simulation are compared with the experimental and numerical results available in Ref. [67]. When the incident shock wave interacts with the panel, reflected and transmitted shock waves appear. We define this instant as $t = 0us$. The time interval for the pictures in Fig. 10 is $70us$. The good agreement of the results can be seen from this figure. Both the shock wave front and vortex induced by the roll-up of the slipstream initiated from the panel trailing end are captured. With increasing time, the motion of the vortex predicted by the present simulation agrees well with the numerical results from Ref. [67].

In Fig. 11, the displacement of the trailing end versus time is compared with available data from the literature. The present results agree well with those predicted by both the simulation and experiment in Ref. [67]. Specifically, both the times when the displacement reaches the peak value and the largest displacement coincide well with the experimental data showing that the present numerical method is accurate and efficient when dealing with FSI problems involving shock waves.

4.5. An inclined flexible plate in a hypersonic flow

In this section, we consider a flexible plate vibrating in a hypersonic flow. As shown in Fig. 12, the structure contains two parts, one is a trangle (solid line) fixed in the flow, the other is the flexible plate (dashed line) which can vibrate under the hypersonic flow load. The flexible part is initially mounted in the flow with an angle α_0 to the horizontal direction. As previously discussed, the turbulence is not considered in this case.

In order to provide validation data, the experiment is conducted in a Ludweig tunnel. The details of the experiment can be found in our previous study [70]. The initial parameters in the low pressure part of

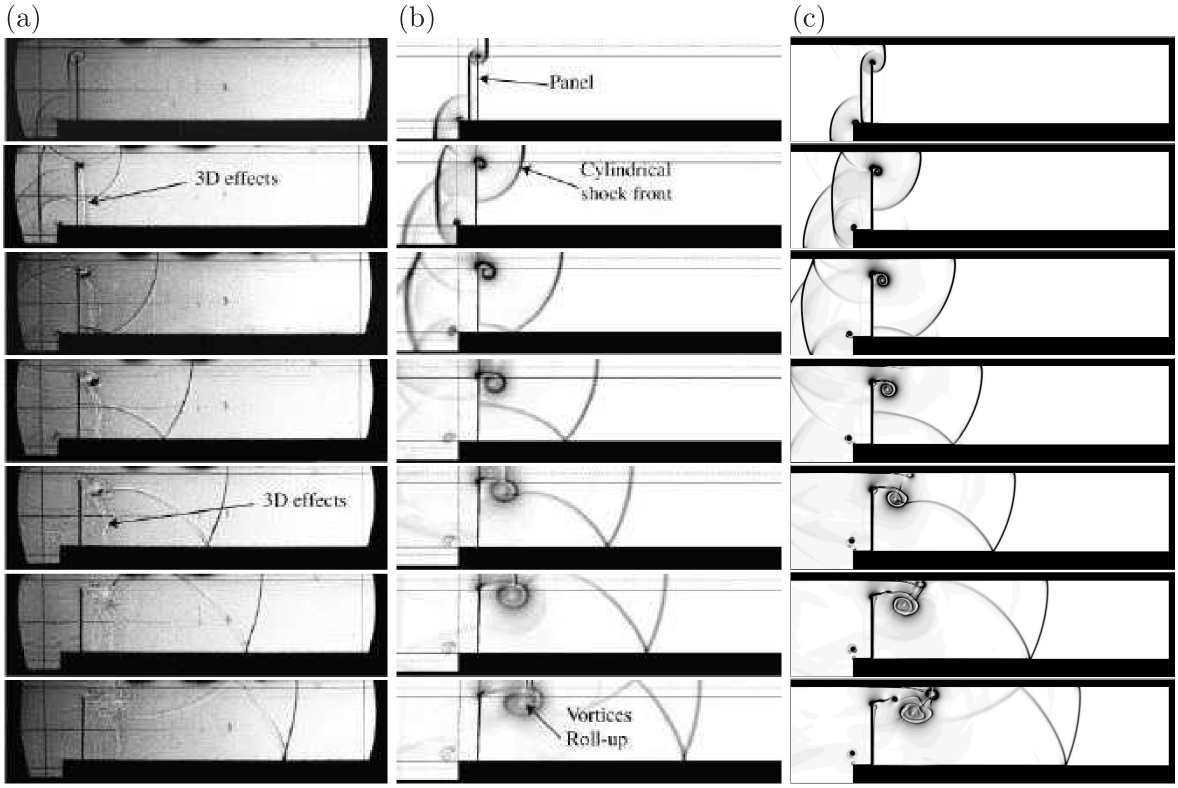

Figure 10: Schlieren pictures: (a) experiment from Ref. [67], (b) simulation from Ref. [67], and (c) present simulation. The time lasts from 0us (when the shock wave impacts on the panel) to 420us with an interval of 70us.

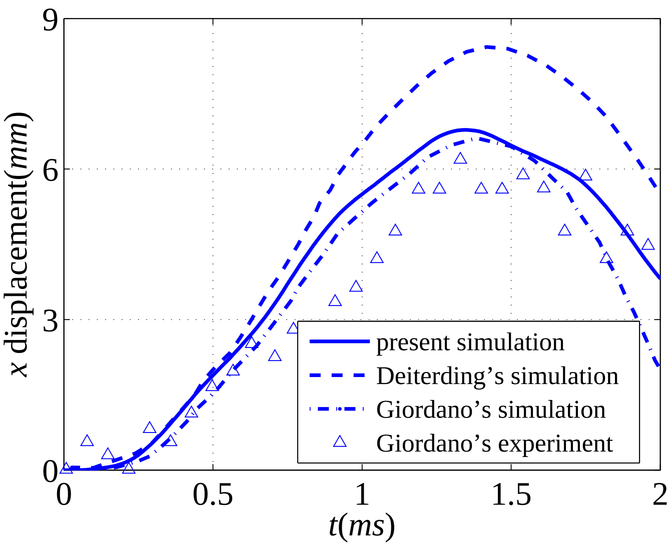

Figure 11: $x-$displacement of the trailing end.

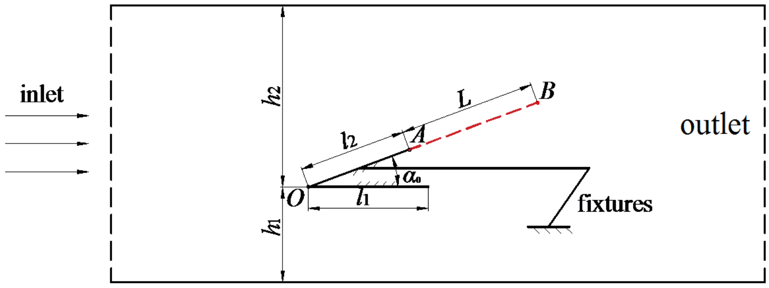

Figure 12: Schematic of a plate in a hypersonic flow. The solid line (OA) is the fixed part and the dashed line (AB) is the flexible plate.

the tunnel are pressure $P_0 = 525Pa$, temperature $T_0 = 294K$, and density $\rho_0 = 6.03 \times 10^{-3}kg/m^3$. The inlet parameters are pressure $P_{in} = 767.6Pa$, velocity $v_{in} = 1000.76m/s$, temperature $T_{in} = 74.08K$, and sound speed $c_{in} = 172.54m/s$. The right-hand side is a free outflow boundary. The plate is initially mounted on a $20°$ rigid wedge. The length L, width w and thickness are respectively $130mm$, $80mm$ and $2mm$. The material of the plate is $AL6061 - T6$, for which the density $\rho = 2700kg/m^3$, elasticity modulus $E_0 = 68.9GPa$, and Poisson's ratio $\nu = 0.33$. Other geometric parameters defined in Fig. 12 are $\alpha_0 = 20°$, $l_1 = 160mm$ and $l_2 = 100mm$.

In the experiment, the high-speed camera is used to record the displacement of the trailing end (B point), and a pressure transducer is attached on the top surface of the plate at point B to obtain the pressure time histories. By using the present numerical method, we conduct an equivalent two-dimensional simulation to compare with the experiment. In the simulation, we use L, ρ_{in} and c_{in} to nondimensionalize the parameters. The non-dimensional inlet parameters are Mach number $M^*_{in} = 5.8$, pressure $P^*_{in} = 0.7142$, and density $\rho^*_{in} = 1.0$. The initial non-dimensional properties of the computational domain are $\rho^*_0 = 0.1662$ and $P^*_0 = 0.4885$. The non-dimensional parameters of the plate are tension rigidity $K^*_S = 9.86 \times 10^5$, bending rigidity $K^*_B = 21.83$ and mass ratio $\rho^*_s = 1150.65$. The non-dimensional geometric parameters are $l_1 = 1.23$ and $l_2 = 0.77$. The computational domain extends from $(-1.77L, -1.77L)$ to $(7.08, 1.77L)$, and the endpoint of the edge O is initially located at $(0, -0.24L)$. We use $0.01L$ and $0.005L$ mesh size for the fluid and plate, respectively. The fixtures defined in Fig. 12 are ignored in the simulation.

We present the calculated $y-$coordinate of the trailing end together with the experimental result in Fig. 13. The oscillating periods from the simulation and experiment are about $9.3ms$ and $9.8ms$, respectively. The deviation is about 5.2%. It is found that the simulation amplitude agrees well with the experimental one, especially in the first several oscillating cycles, the discrepancies may due to the two-dimensional simplification in the numerical simulation. The noise of the inlet fluid in experiment can also affect the motion of the plate. Therefore, the initial discrepancies at the first half period are attributed to the initial perturbation of the tunnel, which obviously leads to an initial velocity of the plate before $0ms$ apparent in Fig. 13. However, the present two-dimensional simulation can capture all

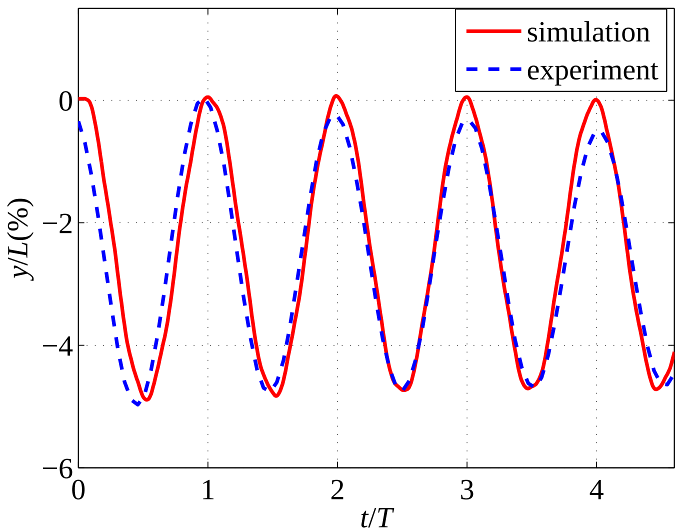

Figure 13: y-coordinate histories of the trailing end of a plate flapping in a hypersonic flow.

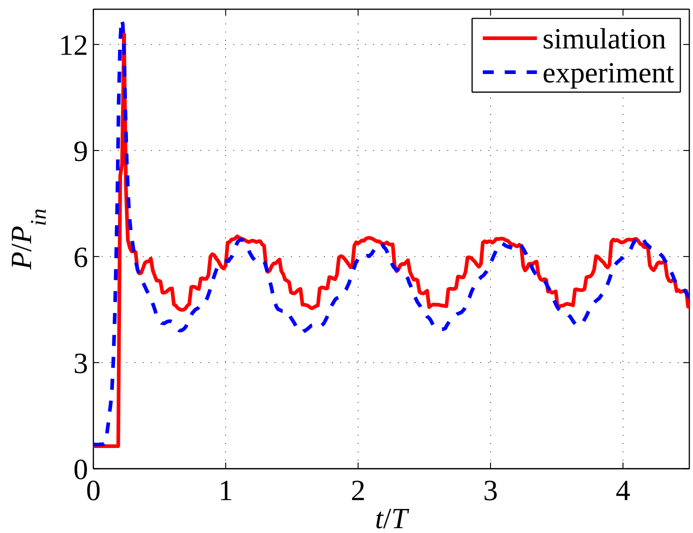

Figure 14: Pressure histories above the trailing end (B) of a flexible plate flapping in a hypersonic flow.

the plate dynamic characteristics observed in the experiment.

The pressure histories of the trailing end (B) are plotted in Fig. 14. As the pressure from the transducer fluctuates violently, a Fourier transform method is used to filter the results. It can be seen that the first pressure peak when the hypersonic flow interacts with the flexible plate has been accurately captured in the numerical simulation. With the vibration of the trailing end of the plate, the pressure oscillation is observed in both simulation and experiment. However, we also found that the minimum

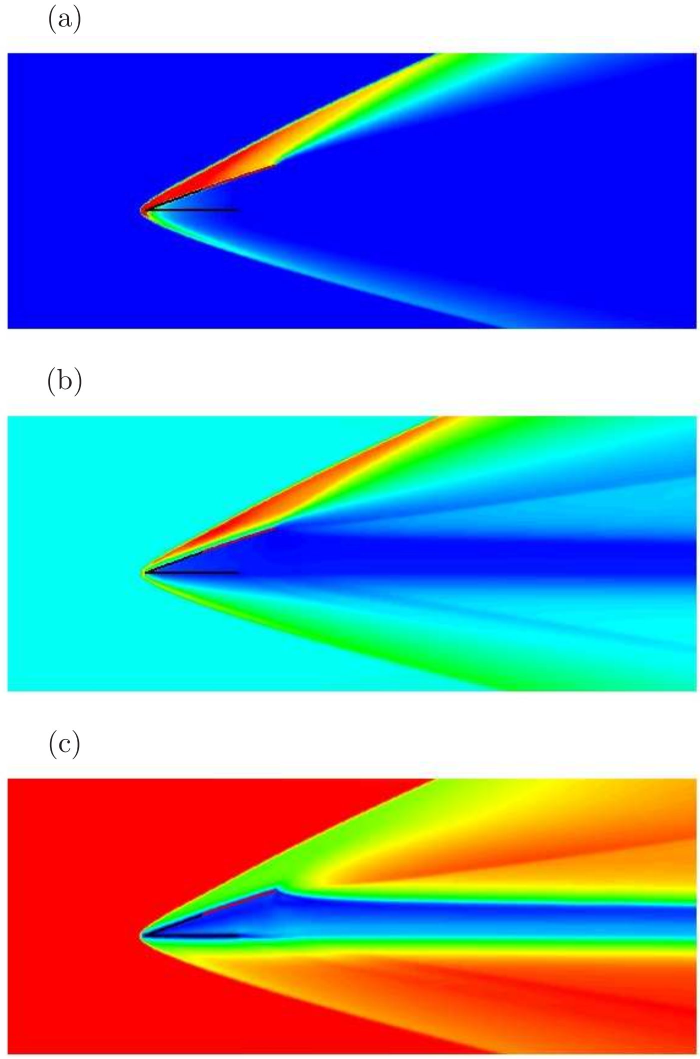

Figure 15: Contours of the non-dimensional pressure (a), density (b) and local Mach number (c), where the pressure ranges from 1.0 to 6.0, the density ranges from 0.1 to 3.6, and the local Mach number ranges from 0 to 5.8.

pressure during the oscillation in the simulation is a little higher than the experimental value. This discrepancy is mostly due to the three-dimensional effects. Fig. 15 shows the pressure, density and local Mach number contours, and Fig. 16 compares the Schlieren pictures obtained from simulation and experiment. It is found that the front shock wave and the rarefactions near the trailing end of both the flexible plate and the rigid fixture are well captured. Therefore, the numerical results are in good agreement with the experimental data.

In order to get a larger deformation of the flexible plate, we simulate a more flexible case where the thickness of the plate is $1mm$. It should be noted that the deformation of the plate is assumed to be elastic in the simulation, while the steel plate might undergo plastic deformation with such thickness. In Fig. 17, the y-coordinate time histories of the trailing end of the plate are presented. It is found that the

(a) (b)

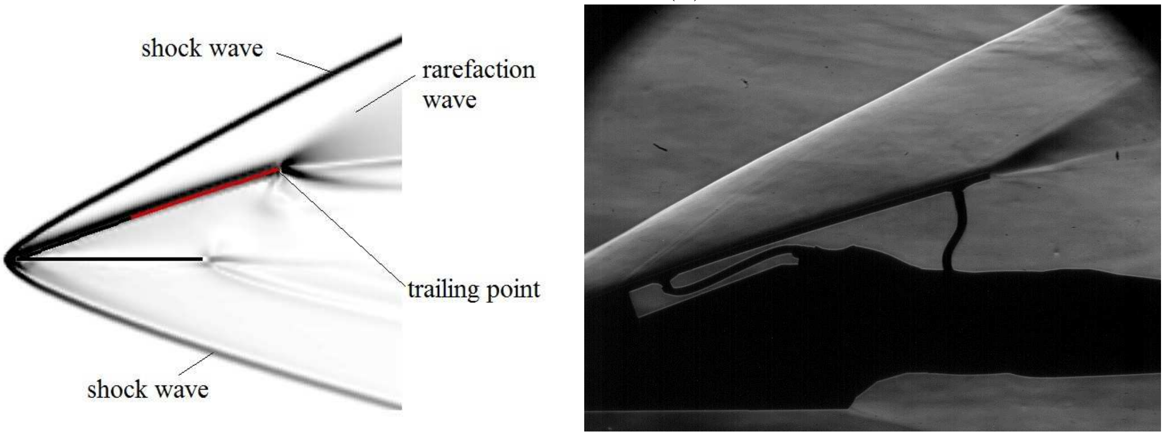

Figure 16: Schlieren pictures from simulation (a) and experiment (b) at time 25ms.

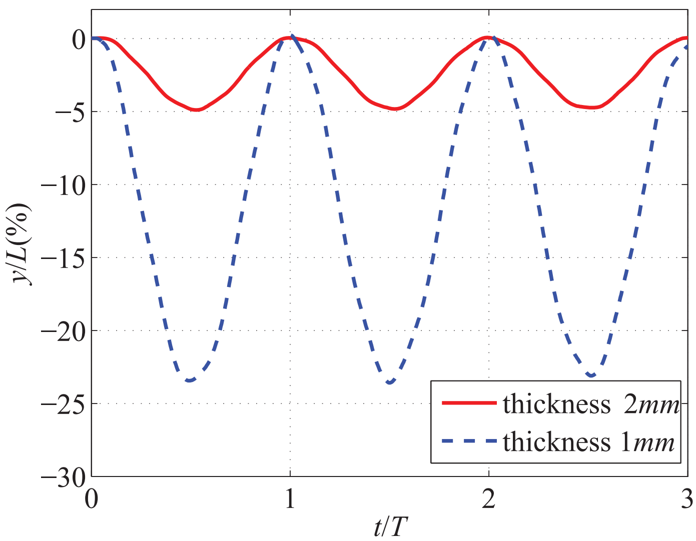

Figure 17: y-coordinate time histories of the trailing end of two flexible plates. The periods are respectively $20.5ms$ (thickness $1mm$) and $9.4ms$ (thickness $2mm$).

amplitude and period increase remarkably, due to the fact that the bending rigidity drops significantly with the decrease of thickness. This simulation can be used for numerical validation in the future.

4.6. Shock-induced collapse of a cylinderical helium cavity in the air

In this section, we examine a Mach 1.22 air shock-induced collapse of a cylindrical helium bubble to validate the present multiphase flow solver. The results from both experiments and simulations can be found in Refs. [20, 71]. The computational domain ranges from (-175,-44.5) to (150,44.5) with a mesh size of 0.25, the cylindrical helium bubble is initially set at the origin with a diameter of 25. The air

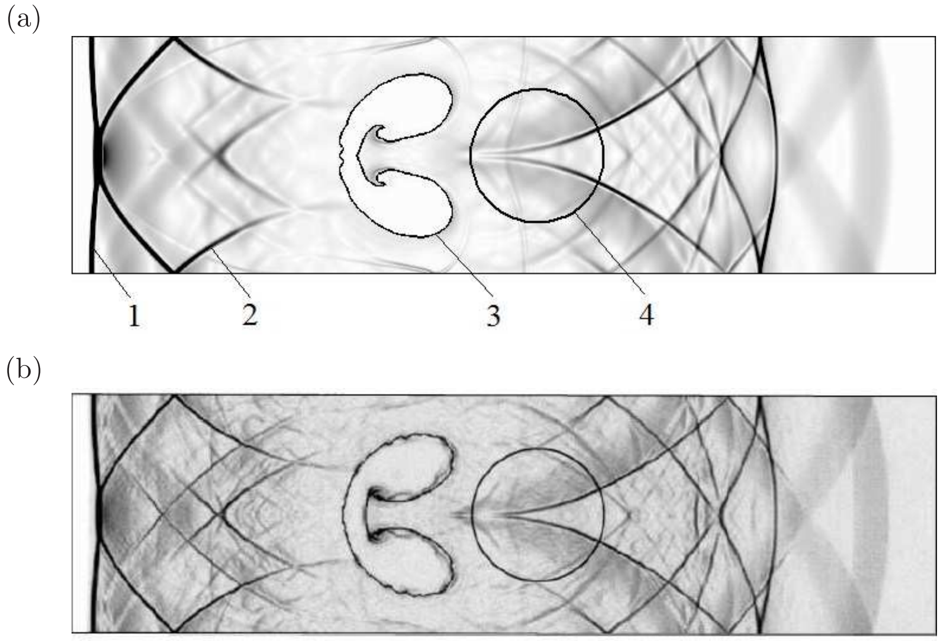

Figure 18: Schlieren pictures from present simulation (a) and Ref. [20] (b) at time $427us$. Where, 1 is the shock wave front, 2 is the reflected wave from the rigid wall, 3 is the current configuration of the bubble, 4 is the initial configuration of the bubble, and other curbes are reflected waves.

is separated into two parts consistent with an initial shock: one ranges from (-175,-44.5) to (0,44.5), and the other one ranges from (0,-44.5) to (150,44.5). The non-dimensional initial parameters of the two parts are $P_I = 1.0$, $\rho_I = 1.0$, $u_I = 1.0$, $v_I = 0.0$, $P_{II} = 1.5698$, $\rho_{II} = 1.3764$, $u_{II} = -0.394$, $v_{II} = 0.0$, and $\gamma = 1.4$. The initial state of the helium bubble is set as $P_b = 1.0$, $\rho_b = 0.138$, $u_b = 0.0$, $v_b = 0.0$, and $\gamma_b = 1.67$. The top and bottom walls are no-slip boundary and the incident shock wave propagates from right to left. The Schlieren pictures from both present simulation and Ref. [20] at time $427us$ are presented in Fig. 18. We can see the good agreement of both results. The wave fronts are clearly captured and the deformation of the helium bubble is predicted well. The comparisons of bubble shapes and waves show that the current results are in good agreement with previous numerical data from Ref. [20].

5. Applications

5.1. A flexible plate interacting with a multiphase flow

As the first application, we consider a flexible plate interacting with a multiphase flow. The computational schematic is shown in Fig. 19, where two different materials are initially filled in the left-hand and right-hand parts of the tube, respectively, and the flexible plate is initially placed right at the multi-material interface with one end fixed. When the simulation starts, the high pressure and material I on the left-hand side transit to the right-hand side, and impact on the flexible plate. Again as the

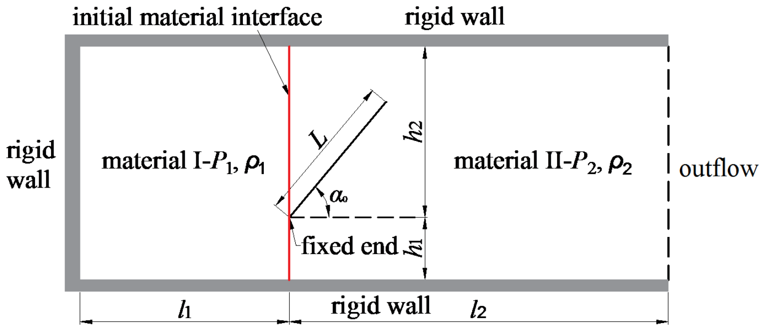

Figure 19: Schematic of an inclined plate interacting with a multiphase flow.

simulation is started from quiescent conditions and total duration is relatively short, turbulence does not play a dominating role this problem and is not considered.

The initial state of material II in the tube is set as $\rho_{II} = 1.22kg/m^3$, $P_{II} = 1.01 \times 10^3 KPa$, and $\gamma_{II} = 2.0$. The length of the plate is $L = 1.0m$. We use the initial parameters of material II including ρ_{II}, c_{II} and L to non-dimensionlize all parameters. The non-dimensional parameters of the plate (as defined in Section 4.5) are $\rho_s^* = 0.22$, $K_S^* = 485.8$ and $K_b^* = 0.0454$. Other geometric parameters are $l_1 = 2.0$, $l_2 = 3.0$, $h_1 = 0.5$, $h_2 = 1.5$ and $\alpha_0 = 60°$. The mesh size for the fluid and plate are respectively $0.015L$ and $0.01L$.

Three different initial conditions of material I are simulated: (a) $P_I = 2P_{II}$ and $\rho_I = 2\rho_{II}$, (b) $P_I = 5P_{II}$ and $\rho_I = 5\rho_{II}$, and (c) $P_I = 10P_{II}$ and $\rho_I = 10\rho_{II}$. $\gamma_I = 1.4$ is used for all simulations. In Fig. 20, the calculated coordinate histories of the trailing end in x-direction are presented. As shown in this figure, with increasing initial pressure and density of material I, the deformation of the plate rises significantly. As the pressure propagates faster than the fluid, the trailing end of the plate first undergoes a small deformation in the negative horizontal direction before t/T =0.32 for (a), 0.28 for (b) and 0.25 for (c), under the impact of the pressure on the lower part. Subsequently, after the pressure acts on the whole plate, a significant deformation of the plate is observed. Finally, the inertial force of the denser material I impacts on the plate and leads a farther deformation of the plate. However, we note that the pressure load plays a dominate role on the deformation. On the other hand, the presence of the plate leads to a flow around the plate. As shown in Fig. 21, both the multi-material interface and the motion of the plate at five instants are presented. It is found that the larger pressure induces more significant deformation of the plate and faster flow velocity. However, when the deformation of the plate is smaller, the flow around the plate is much more apparently, because the large deformation of the plate presents less drag effects on material I while it is flowing around the plate.

5.2. Flexible plate moving across a multiphase flow

In this section, a flexible plate moving from one fluid material to another material is considered. The initial state of the materials are density $\rho_I = 5.0, \rho_{II} = 1.0$, pressure $p_I = p_{II} = 1000$, $\gamma_I = 2.0$ and $\gamma_{II} = 1.4$. The non-dimensional parameters are $\rho_s^* = 1.0, K_S^* = 1000, K_b^* = 0.1$ and length of the plate $L = 1.0$. In the simulation, the center point of the flexible plate moves with a fixed velocity.

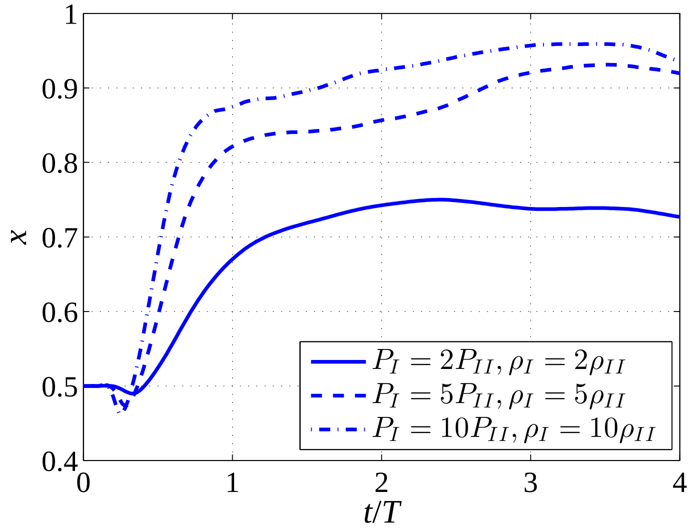

Figure 20: x-coordinate time histories of the trailing end of a plate interacting with multiphase flow in a shock tube. (a) $P_I = 2P_{II}$ and $\rho_I = 2\rho_{II}$, (b) $P_I = 5P_{II}$ and $\rho_I = 5\rho_{II}$, and (c) $P_I = 10P_{II}$ and $\rho_I = 10\rho_{II}$.

Three different velocities are considered: u =1.0,5.0 and 10.0. The computational domain for the fluid is a 4.0×5.0 rectangle, and the plate is initially deployed in material I with a distance of 0.5 from the multi-material interface. The mesh size of the fluid and plate are respectively $0.015L$ and $0.01L$.

In Fig. 22, both the multi-material interface and the motion of the plate at five instants are presented. It is found that with an increase of the velocity, the deformation of the plate augments remarkably, especially when the velocity increases from 1.0 to 5.0. Additionally, while the plate moves from material I to material II, some material I is entrained and mixed with material II. Interestingly the smaller velocity of the plate leads to greater mixture due to the smaller deformation of the plate and the larger associated wake. In Fig. 23, the y-position histories of the trailing end of the plate are plotted, as the motion of both two trailing ends on the plate is symmetric, only the upper trailing end is presented. It clearly shows that how a larger velocity leads to more significant plate bending.

6. Conclusions

We have presented an FSI method based on the penalty immersed boundary method for FSI problems involving shock waves, large structure deformation and multiphase flow. This method consists of three parts: a flow solver based on the high-order finite difference method, a structure solver using the finite element method based on the absolute nodal coordinate formulation, and partitioned fluid–structure interaction coupling using a feed back penalty immersed boundary method.

To validate each component of this solver, we conduct three benchmark cases: a uniform flow around a cylinder for fluid solver, a hanging filament in vacuum for structure solver and flow induced vibration of a high flexible plate in a uniform flow. Results show very good agreement with the published data

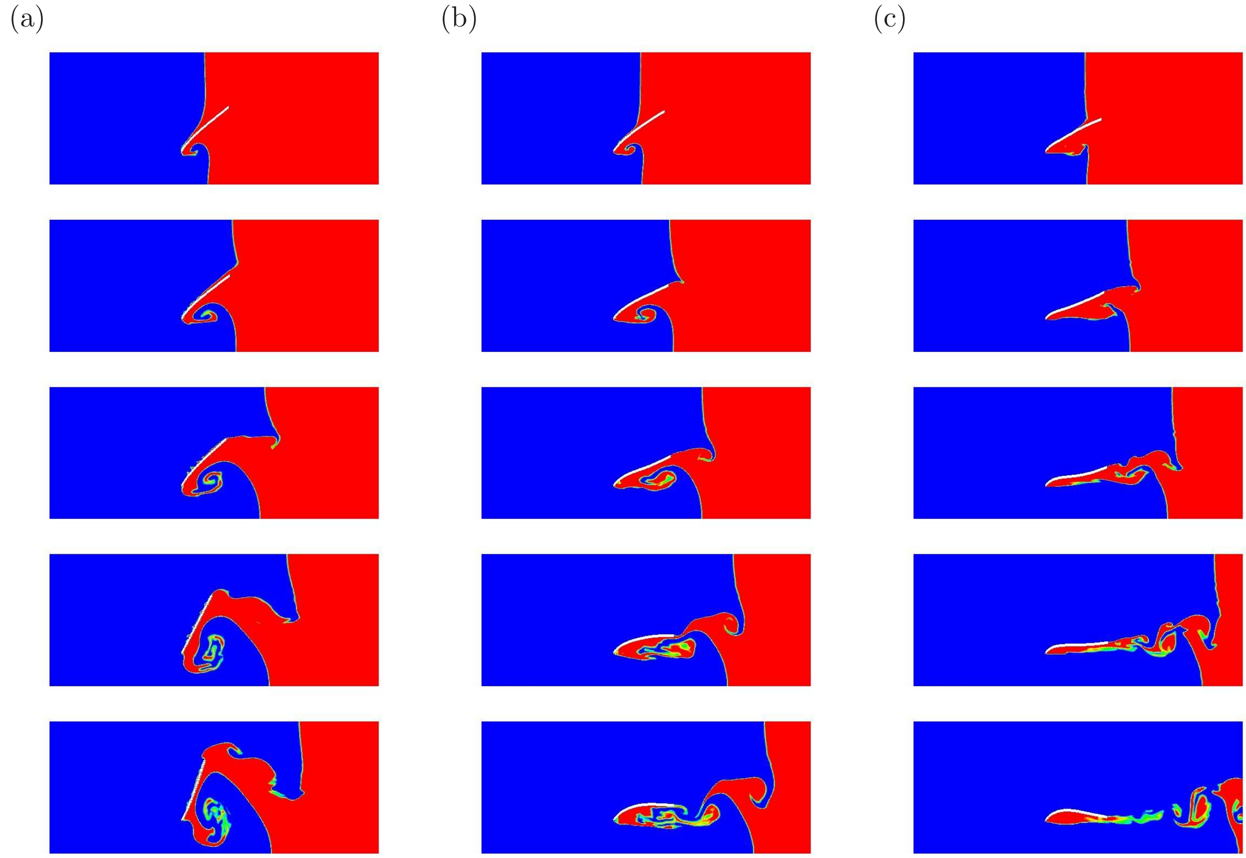

Figure 21: Multi-material interface contour: (a) $P_I = 2P_{II}$ and $\rho_I = 2\rho_{II}$, (b) $P_I = 5P_{II}$ and $\rho_I = 5\rho_{II}$, and (c) $P_I = 10P_{II}$ and $\rho_I = 10\rho_{II}$. The non-dimensional time ranges from 1.6 to 8.0 with an interval of 1.6 in (a), and from 0.8 to 4.0 with an interval of 0.8 in (b) and (c).

predicted by other numerical methods. We further validate our solver by calculating the deformation of a flexible panel induced by a shock wave in a shock tube, an inclined flexible plate in a hypersonic wind tunnel and shock-induced collapse of a cylindrical helium cavity in air. In order to provide validation data, we also conduct an experimental measurement of an inclined flexible plate in a hypersonic wind tunnel. It is found that the results predicted by the present solver agree well with those predicted by other numerical methods and experimental measurements. Finally, we apply the method to calculate two problems: a flexible plate interacting with multiphase flow in a shock tube and a flexible plate moving across a fluid–fluid interface to demonstrate the versatility of the present method. Several sets of governing parameters are considered, and the major dynamic features are captured and discussed. Results can be used as validation cases in future FSI method development.

It should be pointed out that the present solver is based on a two-dimensional uniform mesh. While many merits have been demonstrated by the cases presented, this method is time consuming and does not consider turbulence and gas ionization in the hypersonic flow. Our future work will consider three-dimensional simulations incorporating turbulent models, adaptive mesh refinement and chemical

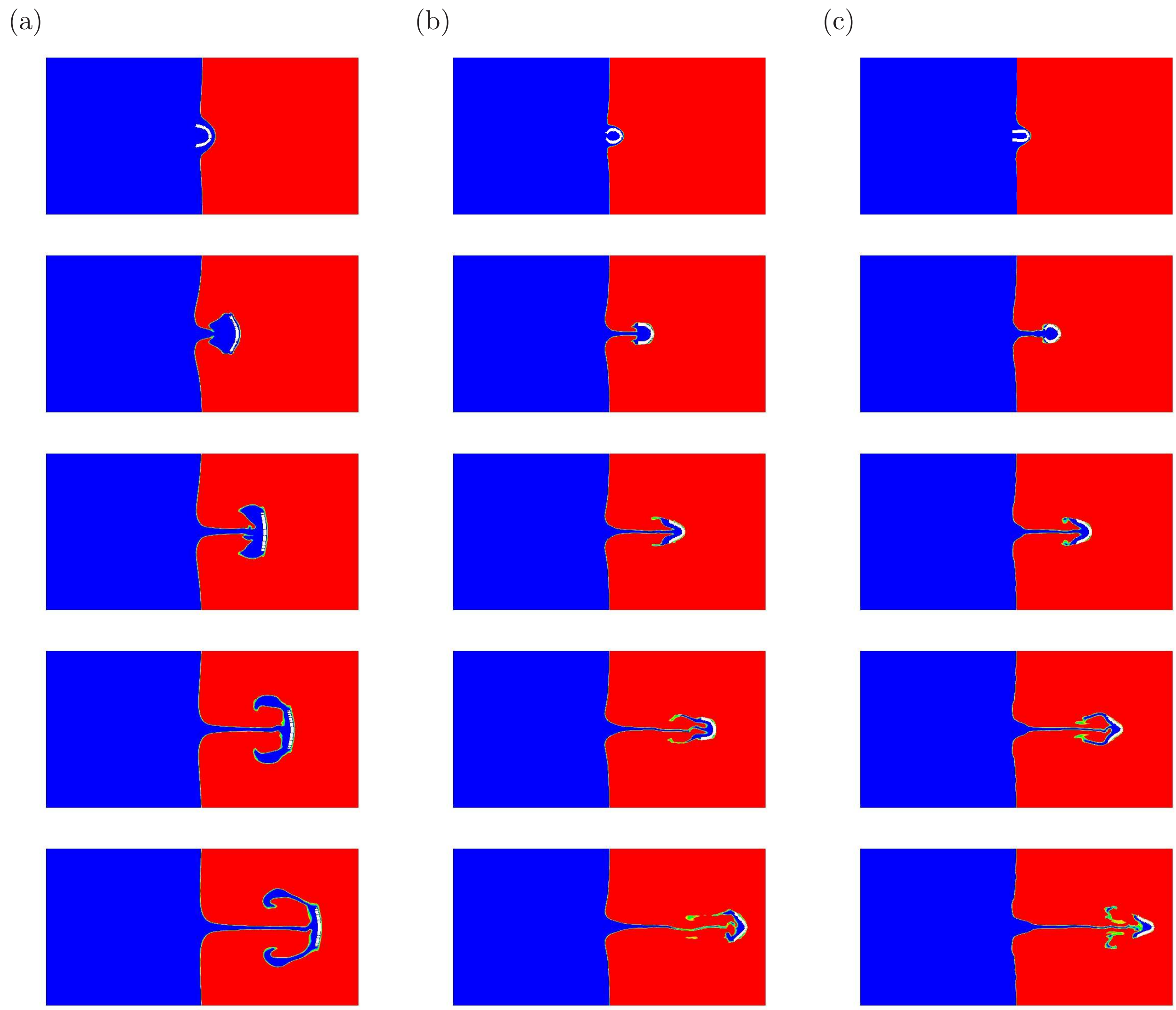

Figure 22: Multi-material interface contours: (a) $u = 1.0$, (b) $u = 5.0$, and (c) $u = 10.0$. The non-dimensional time ranges from 0.7 to 3.5 with an interval of 0.7 in (a), from 0.16 to 0.8 with an interval of 0.16 in (b), and from 0.08 to 0.4 with an interval of 0.08 in (c).

processes.

Acknowledgements

Dr. F.-B. Tian is the recipient of an Australian Research Council Discovery Early Career Researcher Award (project number DE160101098). This research was partially funded by the International Graduate Exchange Program of Beijing Institute of Technology and the Early Career Researcher Grants Scheme, UNSW Canberra.

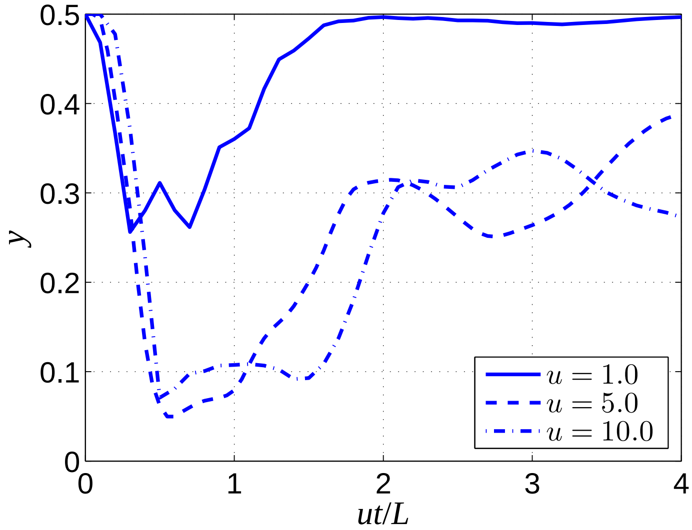

Figure 23: y-coordinate histories of the upper trailing end versus the x-coordinate of the central point on the plate at $u = 1.0$, 5.0 and 10.0.

References

[1] S. Beji, J. Battjes, Numerical simulation of nonlinear wave propagation over a bar, Coastal Engineering 23 (1994) 1–16.

[2] G. Boudier, L. Gicquel, T. Poinsot, D. Bissieres, C. Bérat, Comparison of les, rans and experiments in an aeronautical gas turbine combustion chamber, Proceedings of the Combustion Institute 31 (2007) 3075–3082.

[3] H. Luo, R. Mittal, X. Zheng, S. A. Bielamowicz, R. J. Walsh, J. K. Hahn, An immersed-boundary method for flow–structure interaction in biological systems with application to phonation, Journal of Computational Physics 227 (2008) 9303–9332.

[4] F.-B. Tian, H. Dai, H. Luo, J. F. Doyle, B. Rousseau, Fluid–structure interaction involving large deformations: 3D simulations and applications to biological systems, Journal of Computational Physics 258 (2014) 451–469.

[5] G. F. Kinney, K. J. Graham, Explosive Shocks in Air, Springer Science & Business Media, 2013.

[6] J. J. McNamara, P. P. Friedmann, Aeroelastic and aerothermoelastic analysis in hypersonic flow: past, present, and future, AIAA journal 49 (2011) 1089–1122.

[7] Y. Bazilevs, K. Takizawa, T. E. Tezduyar, Computational fluid-structure interaction: methods and applications, John Wiley & Sons, 2013.

[8] A. Harten, B. Engquist, S. Osher, S. R. Chakravarthy, Uniformly high order accurate essentially non-oscillatory schemes, III, in: Upwind and High-Resolution Schemes, Springer, 1987, pp. 218–290.

[9] A. Harten, S. Osher, Uniformly high-order accurate nonoscillatory schemes. I, SIAM Journal on Numerical Analysis 24 (1987) 279–309.

[10] C.-W. Shu, S. Osher, Efficient implementation of essentially non-oscillatory shock-capturing schemes, Journal of Computational Physics 77 (1988) 439–471.

[11] C.-W. Shu, S. Osher, Efficient implementation of essentially non-oscillatory shock-capturing schemes, ii, in: Upwind and High-Resolution Schemes, Springer, 1989, pp. 328–374.

[12] E. Fatemi, J. Jerome, S. Osher, Solution of the hydrodynamic device model using high-order nonoscillatory shock capturing algorithms, IEEE Transactions on Computer-Aided Design of Integrated Circuits and Systems 10 (1991) 232–244.

[13] C.-W. Shu, Numerical experiments on the accuracy of ENO and modified ENO schemes, Journal of Scientific Computing 5 (1990) 127–149.

[14] G.-S. Jiang, C.-W. Shu, Efficient implementation of weighted ENO schemes., Technical Report, DTIC Document, 1995.

[15] G. Erlebacher, M. Y. Hussaini, C.-W. Shu, Interaction of a shock with a longitudinal vortex, Journal of Fluid Mechanics 337 (1997) 129–153.

[16] E. Weinan, C.-W. Shu, A numerical resolution study of high order essentially non-oscillatory schemes applied to incompressible flow, Journal of Computational Physics 110 (1994) 39–46.

[17] A. Dolezal, S. Wong, Relativistic hydrodynamics and essentially non-oscillatory shock capturing schemes, Journal of Computational Physics 120 (1995) 266–277.

[18] T. Belytschko, B. Hsieh, Non-linear transient finite element analysis with convected co-ordinates, International Journal for Numerical Methods in Engineering 7 (1973) 255–271.

[19] D. Sulsky, Z. Chen, H. L. Schreyer, A particle method for history-dependent materials, Computer methods in applied mechanics and engineering 118 (1994) 179–196.

[20] R. P. Fedkiw, T. Aslam, B. Merriman, S. Osher, A non-oscillatory Eulerian approach to interfaces in multimaterial flows (the ghost fluid method), Journal of Computational Physics 152 (1999) 457–492.

[21] W. Mulder, S. Osher, J. A. Sethian, Computing interface motion in compressible gas dynamics, Journal of Computational Physics 100 (1992) 209–228.

[22] M. Sussman, P. Smereka, S. Osher, A level set approach for computing solutions to incompressible two-phase flow, Journal of Computational Physics 114 (1994) 146–159.

[23] J. Sethian, P. Smereka, Level set methods for fluid interfaces, Annual Review of Fluid Mechanics 35 (2003) 341–372.

[24] T. Liu, B. Khoo, K. Yeo, Ghost fluid method for strong shock impacting on material interface, Journal of Computational Physics 190 (2003) 651–681.

[25] Y.-H. Tseng, J. H. Ferziger, A ghost-cell immersed boundary method for flow in complex geometry, Journal of Computational Physics 192 (2003) 593–623.

[26] C. S. Peskin, Numerical analysis of blood flow in the heart, Journal of Computational Physics 25 (1977) 220–252.

[27] C. S. Peskin, The immersed boundary method, Acta Numerica 11 (2002) 479–517.

[28] H. Bandringa, Immersed Boundary Methods, Master's thesis, University of Groningen 9700 (2010).

[29] W.-X. Huang, S. J. Shin, H. J. Sung, Simulation of flexible filaments in a uniform flow by the immersed boundary method, Journal of Computational Physics 226 (2007) 2206–2228.

[30] R. Mittal, G. Iaccarino, Immersed boundary methods, Annual Review of Fluid Mechanics 37 (2005) 239–261.

[31] L. Zhu, C. S. Peskin, Simulation of a flapping flexible filament in a flowing soap film by the immersed boundary method, Journal of Computational Physics 179 (2002) 452–468.

[32] Y. Kim, C. S. Peskin, Penalty immersed boundary method for an elastic boundary with mass, Physics of Fluids 19 (2007) 053103.

[33] D. Goldstein, R. Handler, L. Sirovich, Modeling a no-slip flow boundary with an external force field, Journal of Computational Physics 105 (1993) 354–366.

[34] R. Ghias, R. Mittal, H. Dong, A sharp interface immersed boundary method for compressible viscous flows, Journal of Computational Physics 225 (2007) 528–553.

[35] Y. Qiu, C. Shu, J. Wu, Y. Sun, L. Yang, T. Guo, A boundary condition-enforced immersed boundary method for compressible viscous flows, Computers & Fluids 136 (2016) 104–113.

[36] M. D. de Tullio, P. De Palma, G. Iaccarino, G. Pascazio, M. Napolitano, An immersed boundary method for compressible flows using local grid refinement, Journal of Computational Physics 225 (2007) 2098–2117.

[37] R. Bhardwaj, R. Mittal, Benchmarking a coupled immersed-boundary-finite-element solver for large-scale flow-induced deformation, AIAA journal 50 (2012) 1638–1642.

[38] F.-B. Tian, H. Luo, L. Zhu, X.-Y. Lu, Interaction between a flexible filament and a downstream rigid body, Physical Review E 82 (2010) 026301.

[39] F.-B. Tian, H. Luo, L. Zhu, X.-Y. Lu, Coupling modes of three filaments in side-by-side arrangement, Physics of Fluids 23 (2011) 111903.

[40] F.-B. Tian, Role of mass on the stability of flag/flags in uniform flow, Applied Physics Letters 103 (2013) 101–104.

[41] J. F. Doyle, Nonlinear analysis of thin-walled structures: statics, dynamics, and stability, Springer Science & Business Media, 2013.

[42] C. Rankin, F. Brogan, An element independent corotational procedure for the treatment of large rotations, Journal of Pressure Vessel Technology 108 (1986) 165–174.

[43] A. A. Shabana, Flexible multibody dynamics: review of past and recent developments, Multibody System Dynamics 1 (1997) 189–222.

[44] A. A. Shabana, Dynamics of Multibody Systems, Cambridge Uuniversity Press, 2013.

[45] A. Shabana, H. Hussien, J. Escalona, Application of the absolute nodal coordinate formulation to large rotation and large deformation problems, Journal of Mechanical Design 120 (1998) 188–195.

[46] B. Chang, A. Shabana, Total lagrangian formulation for the large displacement analysis of rectangular plates, International journal for numerical methods in engineering 29 (1990) 73–103.

[47] A. A. Shabana, Computer implementation of the absolute nodal coordinate formulation for flexible multibody dynamics, Nonlinear Dynamics 16 (1998) 293–306.

[48] A. A. Shabana, A. P. Christensen, Three-dimensional absolute nodal co-ordinate formulation: plate problem, International journal for numerical methods in engineering 40 (1997) 2775–2790.

[49] J. T. Sopanen, A. M. Mikkola, Description of elastic forces in absolute nodal coordinate formulation, Nonlinear Dynamics 34 (2003) 53–74.

[50] F.-B. Tian, H. Luo, L. Zhu, J. C. Liao, X.-Y. Lu, An efficient immersed boundary-lattice Boltzmann method for the hydrodynamic interaction of elastic filaments, Journal of Computational Physics 230 (2011) 7266–7283.

[51] W.-X. Huang, H. J. Sung, Three-dimensional simulation of a flapping flag in a uniform flow, Journal of Fluid Mechanics 653 (2010) 301–336.

[52] P. De Palma, M. De Tullio, G. Pascazio, M. Napolitano, An immersed-boundary method for compressible viscous flows, Computers & Fluids 35 (2006) 693–702.

[53] X.-D. Liu, S. Osher, T. Chan, Weighted essentially non-oscillatory schemes, Journal of Computational Physics 115 (1994) 200–212.

[54] M. Berzeri, M. Campanelli, A. A. Shabana, Definition of the elastic forces in the finite-element absolute nodal coordinate formulation and the floating frame of reference formulation, Multibody System Dynamics 5 (2001) 21–54.

[55] M.-C. Lai, C. S. Peskin, An immersed boundary method with formal second-order accuracy and reduced numerical viscosity, Journal of Computational Physics 160 (2000) 705–719.

[56] M. N. Linnick, H. F. Fasel, A high-order immersed interface method for simulating unsteady incompressible flows on irregular domains, Journal of Computational Physics 204 (2005) 157–192.

[57] D. Russell, Z. J. Wang, A cartesian grid method for modeling multiple moving objects in 2D incompressible viscous flow, Journal of Computational Physics 191 (2003) 177–205.

[58] K. Herfjord, A study of Two-dimensional Separated Flow by a Combination of the Finite Element Method and Navier-Stokes equations, Doctor's thesis, Norwegian Institute of Technology 9700 (1996).

[59] P. A. Berthelsen, O. M. Faltinsen, A local directional ghost cell approach for incompressible viscous flow problems with irregular boundaries, Journal of Computational Physics 227 (2008) 4354–4397.

[60] S. Xu, Z. J. Wang, An immersed interface method for simulating the interaction of a fluid with moving boundaries, Journal of Computational Physics 216 (2006) 454–493.

[61] C. Williamson, Oblique and parallel modes of vortex shedding in the wake of a circular cylinder at low reynolds numbers, Journal of Fluid Mechanics 206 (1989) 579–627.

[62] D.-V. Le, B. C. Khoo, J. Peraire, An immersed interface method for viscous incompressible flows involving rigid and flexible boundaries, Journal of Computational Physics 220 (2006) 109–138.

[63] D. Calhoun, A cartesian grid method for solving the two-dimensional streamfunction-vorticity equations in irregular regions, Journal of Computational Physics 176 (2002) 231–275.

[64] F.-B. Tian, FSI modeling with the DSD/SST method for the fluid and finite difference method for the structure, Computational Mechanics 54 (2014) 581–589.

[65] J. Wu, C. Shu, An improved immersed boundary-lattice Boltzmann method for simulating three-dimensional incompressible flows, Journal of Computational Physics 229 (2010) 5022–5042.

[66] B. S. Connell, D. K. P. Yue, Flapping dynamics of a flag in a uniform stream, Journal of Fluid Mechanics 581 (2007) 33–67.

[67] J. Giordano, G. Jourdan, Y. Burtschell, M. Medale, D. Zeitoun, L. Houas, Shock wave impacts on deforming panel, an application of fluid-structure interaction, Shock Waves 14 (2005) 103–110.

[68] R. Deiterding, F. Cirak, S. P. Mauch, Efficient fluid-structure interaction simulation of viscoplastic and fracturing thin-shells subjected to underwater shock loading, in: International Workshop on Fluid-Structure Interaction. Theory, Numerics and Applications, Kassel University Press GmbH, p. 65.

[69] R. Deiterding, S. Wood, Parallel adaptive fluid–structure interaction simulation of explosions impacting on building structures, Computers & Fluids 88 (2013) 719–729.

[70] G. Currao, A. J. Neely, D. R. Buttsworth, R. Choudhury, Measurement and simulation of hypersonic fluid-structural interaction on a cantilevered plate in a mach 6 flow, in: 15th Dynamics Specialists Conference, p. 1088.

[71] J.-F. Haas, B. Sturtevant, Interaction of weak shock waves with cylindrical and spherical gas inhomogeneities, Journal of Fluid Mechanics 181 (1987) 41–76.